Acta Astronautica 188 (2021) 367–386

Contents lists available at ScienceDirect

Acta Astronautica

journal homepage: www.elsevier.com/locate/actaastro

Research paper

Late-time small body disruptions for planetary defense

Patrick K. King [a,b,c,*], Megan Bruck Syal [b], David S.P. Dearborn [b], Robert Managan [b], J. Michael Owen [b], Cody Raskin [b]

[a] Johns Hopkins University Applied Physics Laboratory, 11100 Johns Hopkins Road, Laurel, MD 20723, United States of America
[b] Lawrence Livermore National Laboratory, 7000 East Avenue, Livermore, CA 94550, United States of America
[c] Department of Astronomy, University of Virginia, 130 McCormick Road, Charlottesville, VA, 22904, United States of America

ARTICLE INFO

Keywords:
Planetary defense
Catastrophic disruption
Potentially hazardous asteroids (PHAs)
Celestial mechanics
N-body simulations

ABSTRACT

Diverting hazardous small bodies on impact trajectories with the Earth can in some circumstances be impossible without risking disrupting them. Disruption is a much more difficult planetary defense scenario to assess, being linked both to the response of the body to shock loading and the much more complicated gravitational dynamics of the fragments in the solar system relative to pure deflection scenarios. In this work we present a new simulation suite built on *N*-body gravitational methods that solves fragment orbits in the full gravitational system without recourse to more approximate methods. We assess the accuracy of our simulations and the simplifying assumptions we adopt to make the system tractable, and then discuss in more detail several specific, plausible planetary defense scenarios based on real close encounters. We find that disruption can be a very effective planetary defense strategy even for very late (sub-year) interventions, and should be considered an effective backup strategy should preferred methods, which require long warning times, fail.

1. Introduction

Collisions between the Earth and small objects in the solar system are known to occur regularly [1], and can result in extinction-level events at their most energetic [2] or more commonly widespread loss of life or economic destruction even for relatively low-energy impacts [3,4]. The field of planetary defense has emerged to develop means to detect and anticipate potential impacts and provide methods to avert them if necessary, and plan for consequence assessment and emergency response if these efforts fail [5]. For mitigation efforts, it is always desirable to know several decades in advance of an impact, as a long warning time requires only a relatively small velocity change to cause the object to miss the Earth. However, such long warning times cannot be guaranteed with current or even near future telescopic facilities, and even with adequate observational resources, obtaining orbit determination that is sufficiently accurate to establish whether impact will occur is challenging [6]. As a result, it is important that the technologies used to avert a possible impact be robust and of mature technological development to ensure mitigation is achievable using existing launch capabilities for the widest range of possible threats [5].

In this context, nuclear explosives remain an indispensable element of the planetary defense portfolio. These devices are uniquely capable of deflecting or disrupting small bodies whose sizes are beyond the current limits of kinetic impactors, the use of which is the generally preferred mitigation method of choice [5]. Purely from the standpoint of mitigation effectiveness, nuclear explosives are known to be highly effective [7–13]. As the time before impact becomes very short, the required energy coupling to the threatening body becomes large enough that fragmentation may be unavoidable, particularly for weakly bound targets; it is suspected that such bodies may constitute a significant sub-population of solar system small bodies [14,15]. Previous work has established that limitations on the nuclear explosive yield are necessary to avoid disrupting the target [8]. An unintentional disruption presents several hazards and uncertainties, including the incomplete disruption of a target, potentially resulting in multiple impacts; but if robust enough, disruption is a viable planetary defense strategy on its own. By simultaneously imparting a center-of-mass impulsive orbit maneuver to all of the fragments and by dispersing the shattered fragments over a much greater volume in their center-of-mass frame, a robust disruption could potentially nullify the impact risk from a hazardous body, or perhaps greatly reduce the scale of the destruction should the fragments still hit the Earth — even for very late interventions. The scenarios we consider here are focused on these types of late warning efforts, in which policymakers do not have the luxury of a long time before impact to intervene. Though some work has been done on last-ditch efforts [16], we focus on times-to-impact of at least one week; such

* Corresponding author at: Johns Hopkins University Applied Physics Laboratory, 11100 Johns Hopkins Road, Laurel, MD 20723, United States of America.
E-mail address: Patrick.King@jhuapl.edu (P.K. King).

https://doi.org/10.1016/j.actaastro.2021.07.034
Received 8 March 2021; Received in revised form 13 July 2021; Accepted 22 July 2021
Available online 31 July 2021

scenarios are consistent with emergency scenario planning for a follow-up nuclear disruption mission should more preferred methods fail to achieve a successful deflection.

More specifically, in this work we aim to quantitatively assess the risks and performance of these late-term disruption planetary defense strategies. Our focus is on following to a high degree of accuracy the orbits of the fragments following the disruption of a hazardous body on an Earth-impact trajectory, and if they result in any Earth impacts, estimate the scale of the consequences. Previous work has attacked this problem using more approximate methods, including the Gauss' planetary equations alongside a state transition matrix approach [17] and the Clohessy–Wiltshire–Hill equations [9,18–20], often augmented with mutual gravitational terms. We aim to drive these efforts forward by implementing tools built around N-body gravity simulations that follow fragment orbits under realistic solar system conditions and ephemerides. These tools will allow quantitative, high-fidelity assessment of the impact risks associated with disrupting a hazardous body. Our assessment cannot be regarded as a fully calibrated risk assessment due to the unavoidable uncertainties in target properties and the approximations made in our simulation strategy. However, we do find that disruption is a highly effective strategy for a range of impactor orbits even for late warning times, provided that the disruption is robust enough. Though any real scenario must be evaluated using more targeted analysis than is provided here, it is our goal to provide improved results that can serve as an even better guide for policymakers and scientists within the planetary defense community in evaluating robust small body disruption strategies for use.

The structure of this paper is as follows. We use a fiducial simulated nuclear explosive scenario to establish some baseline properties of a prototypical fragment field following such an event, which serves as the basis for our choices of initial conditions for our simulations (Section 2). Next we describe the structure of our N-body simulations (Section 3) including the basic physics and simulation elements (Section 3.1); how we select hazardous orbits (Section 3.2); how we avoid close encounter errors and incorporate gravitational focusing (Section 3.3); how we approximate the initial conditions from Section 2 and treat fragment reaccumulation and fragment self-gravity (Section 3.4); what scenarios we consider (Section 3.5); and the drift in our simulations and their range of validity (Section 3.6). Next we discuss the structure of our scenario assessments (Section 4.1); discuss our primary figures of merit, impact fraction and impact energy (Section 4.2); discuss each of the scenarios discussed in Section 3.5 as case studies (Sections Section 4.3 though 4.7); and then discuss several themes from these case studies (Section 4.8). Lastly we summarize our conclusions (Section 5).

2. Numerical disruption study

2.1. Nuclear disruption in Spheral++

For reference, we will present a single 3D disruption study conducted using the Adaptive Smoothed-Particle Hydrodynamics (ASPH) code, Spheral++[1] [21,22]. SPH is a particle-based Lagrangian formalism [23] that is well-suited to modeling material strength and fragmentation [24]. ASPH extends the SPH paradigm by adopting tensor generalizations of the smoothing kernel, which can help preserve accuracy in material behavior at high strain rates with superior zone scaling performance [21,24]. Spheral++ uses a compatibly-differenced total energy-conserving scheme, and has several solid material models and equations of state built-in, among other physics modules. Spheral++ has been used to model both kinetic impactor [12,25,26] and nuclear explosive scenarios [10,12], as well as crater formation [27,28] and catastrophic collisional disruption events [29,30] in previous work.

[1] Spheral++ is available at https://github.com/LLNL/Spheral.

Table 1
Simulation parameters adopted for the equation of state, strength, and porosity models in the numerical disruption study.

Tillotson Equation of State [31]			
Tillotson Parameters	a	0.5	–
	b	1.3	–
(Equal to Bulk Modulus)	A	18	GPa
	B	18	GPa
	α	5.0	–
	β	5.0	–
Reference Specific Energy Density	ϵ_0	1.6×10^{11}	erg/g
Specific Energy Density of Incipient Vaporization	ϵ_{iv}	3.5×10^{10}	erg/g
Specific Energy Density of Complete Vaporization	ϵ_{cv}	1.8×10^{11}	erg/g
Strength Model [32]			
Zero-Pressure Shear Strength	Y_0	100	MPa
von Mises Plastic Limit	Y_M	1.5	GPa -
Coefficient of Internal Friction	μ_i	1.2	–
Porosity Model [33]			
Elastic–Plastic Transition Strain	ϵ_e	0.0	–
Power-Law Transition Strain	ϵ_X	−0.4	–
Exponential Compaction Rate	κ	0.8	–

A ∼20% length-scaled shape model of 101955 Bennu [34] corresponding to a 100-meter diameter asteroid was selected as a target model. The target body was assumed to be a monolithic, uniform density body composed exclusively of SiO_2 (full density 2.68 g cm^{-3}) with a microporosity ϕ of 0.25 (corresponding to bulk density 2.01 g cm^{-3}), with a final target mass of 1.3649×10^{12} grams. The Tillotson equation of state [31,35] was chosen for the material, consistent with standard practice in the field. Though asteroids are not composed of pure SiO_2, the grain density is consistent with chondritic meteorite samples, and differences between various equation of state choices for rocky materials have been shown to be small in previous studies [25]. The Tillotson equation of state has two parts. The first applies when the material is under compression (density greater than the reference material density ρ_0) and is also used for cold expanded states ($\rho < \rho_0$) when the specific energy density is less than the specific energy density of incipient vaporization, ϵ_{iv} [31]:

$$P = \left[a + \frac{b}{\frac{\epsilon}{\epsilon_0}\left(\frac{\rho}{\rho_0}\right)^{-2} + 1} \right] \rho\epsilon + A\left(\frac{\rho}{\rho_0} - 1\right) + B\left(\frac{\rho}{\rho_0} - 1\right)^2, \tag{1}$$

where P is the pressure, ϵ is the specific energy density, a, b, A, and B are the Tillotson parameters, and ϵ_0 is the reference specific energy density. It can be shown [31] that A is equal to the bulk modulus of the material. In the expanded state ($\rho < \rho_0$) where the energy density is greater than the specific energy density of complete vaporization ϵ_{cv}, then the Tillotson equation of state takes the form

$$P = a\rho\epsilon + \left[\frac{b\rho\epsilon}{\frac{\epsilon}{\epsilon_0}\left(\frac{\rho}{\rho_0}\right)^{-2} + 1} + A\left(\frac{\rho}{\rho_0} - 1\right) e^{-\beta\left(\frac{\rho_0}{\rho} - 1\right)} \right] e^{-\alpha\left(\frac{\rho_0}{\rho} - 1\right)^2} \tag{2}$$

where α and β are parameters chosen that control how the equation of state converges to the ideal gas form, $P \propto \rho\epsilon$ [35]. States in which the specific energy density is between ϵ_{iv} and ϵ_{cv} are interpolated using a monotonic cubic to ensure continuity in the derivatives; linear interpolation can introduce undesirable ringing.

The material strength model adopted was a pressure-dependent strength model of the form [32,36,37]:

$$Y = Y_0 + \frac{\mu_i P}{1 + \frac{\mu_i P}{Y_M - Y_0}}, \tag{3}$$

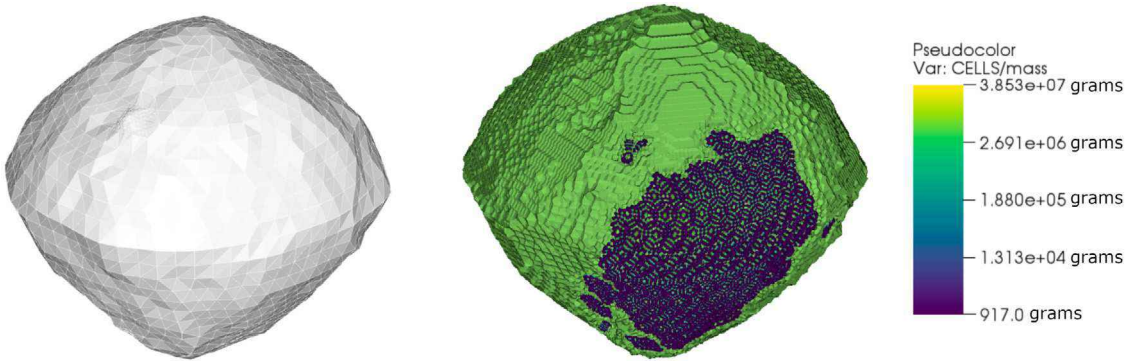

Fig. 1. Left: shape model of 101955 Bennu used for the disruption simulation. Right: the simulation zoning, with SPH particle mass (corresponding to resolution) in color (log-scale); volume indicates the Voronoi cell over which the particle is interpolating hydrodynamics fields. Lower mass zones indicate the high-resolution surface zones resolving the irradiated material. (For interpretation of the references to color in this figure legend, the reader is referred to the web version of this article.)

where Y is the shear modulus, Y_0 is the zero-pressure shear modulus, P is the pressure, Y_M is the von Mises plastic limit of the material, and μ_i is the coefficient of internal friction. Microporosity is modeled in Spheral++ using an ϵ-α scaling of the equation of state and strength [33], which includes an elastic regime, an exponential compaction regime, and a power-law compaction regime. With the bulk and shear moduli defined, the material has a complete homogeneous and isotropic strength prescription. The porosity model parameters were the elastic–plastic transition strain ϵ_e, the power-law transition strain ϵ_X, and the exponential compaction rate κ. The choices made for model parameters can be found in Table 1 and are consistent with work previously published in [25]. Though Spheral++ is capable of modeling material damage and fracture [24], for computational efficiency we do not include this capability in our simulation. This assumption is equivalent to asserting that the post-shock state of the fragments is largely determined by its hydrodynamic history in the high-impulse limit, and that the details of fragmentation primarily affect the sizes of the fragments rather than their speed. This limit is reasonable for low-strength or low-cohesion materials, in which the fracture surface energy is small compared to the energy of the shock. We note that while these choices of parameters are reasonable given known properties of typical NEOs, there may be wide variations in composition, material properties, and internal structure within the hazardous body population that can affect the outcome of these calculations; many small bodies are known to be or suspected of being *rubble piles*, assemblages of material with little cohesive strength and high macroporosity [14,15,38]. Less is known about the typical structure of smaller bodies of the size we are simulating here, as material strength begins to dominate over gravity at these scales; a competent monolithic structure of the type assumed here might be reasonable, but we caution that there is sufficient uncertainty in these properties that precise predictions still require much more definitive characterization.

The target was zoned such that the bulk region of the target had a constant linear resolution of 1.6 m. The code identifies the facets of the shape model that are irradiated by the device, and replaces the constant resolution regions at and below these facets (up to 10 meters in depth) with a higher resolution that is capable of resolving the energy deposition profile. This is done by demanding a surface resolution of 50 μm and using a zoning ratio that gradually adjusts the radial zone resolution until the resolution is roughly mass-matched to that of the bulk region of the target. The total mass of bulk particles is 9.46×10^{11} grams, about 69% of the total mass; the remainder of the mass is in the ablation zone. The zoning is chosen such that the azimuthal/polar resolution is approximately 2 meters at the surface in the ablation region. Ultimately, 233321 individual SPH particles were generated and used in the simulation. Fig. 1 shows the shape model chosen and the initial zoning of the target.

A single 1 MT TNT equivalent device was selected for the disruption event to provide a reasonable but vague value at the higher end of yield, with a standoff height-of-burst of 15 meters above the equator (65 meters from the center) of the target. Height-of-burst is known to affect disruption performance, and optimal selection is size and shape dependent; we chose this height-of-burst to maximize irradiated area without being too affected by shape model details. The device is modeled to be a prompt source of soft thermal (~keV) x-rays whose deposition profile in granite is given in [39]; this modeling approach is the same chosen by the LLNL team in [12]. For every SPH particle in the simulation, the initial specific energy density is given by

$$\epsilon = \frac{\eta(1-f)Y}{4\pi r^2 \rho}\Phi(d)\cos\theta, \tag{4}$$

where Y is the device yield; ρ is the mass density; r is the distance from the source; θ is the angle of incidence; η is the yield coupling, assumed to be 1 for soft x-rays; f is the reradiation fraction; d is the depth from the surface; and Φ is the energy deposition profile with depth. The reradiation fraction is the fraction of deposited energy lost to space by thermal emission prior to hydrodynamic motion, which we chose to be 0.65 to be consistent with radiation hydrodynamics simulations carried out to estimate this number (see, e.g., [12].) The total delivered yield (after reradiation) to the target was 60.5728 kT TNT equivalent. Once initialized the simulation is allowed to evolve hydrodynamically under these energy deposition initial conditions. The simulation was run until it reached a simulation physical time of 0.5 s; the simulation has not completely finished hydrodynamic evolution at this point in time, but particle velocities have begun to approach their asymptotic values.

2.2. Characterization of the disruption simulation results

Of the delivered energy total, 32.184 kT TNT was ultimately converted into the kinetic energy of the finely-zoned particles in the ablation region (about 53.1% of the delivered yield and 3.22% of the total device yield) and 3.858 kT TNT was converted into the coarsely-zoned bulk particle kinetic energy (about 6.37% of the delivered yield and 0.3486% of the total device yield); the remainder of the delivered yield is lost, in a mechanical sense, to the internal energy (heat) of the material that was not converted to kinetic energy. The disruption efficiency can be estimated by computing an estimated kinetic energy per target mass and comparing against Q^*_D, the energy per target mass threshold for catastrophic disruption [40,41]. For bulk particles only,[2] this number is 17047.3 J/kg, significantly larger than the Q^*_D values reported in [40] for targets of equivalent size. We note that the Q^*_D values reported in previous work have focused entirely on large impact studies rather than a nuclear explosive mechanism, so though we do

[2] Inclusion of ablation zone particles significantly increases the estimate of Q^*_D; however, since we assume the ablation zone does not contribute to the large fragments, as noted below, we quote the more conservative number.

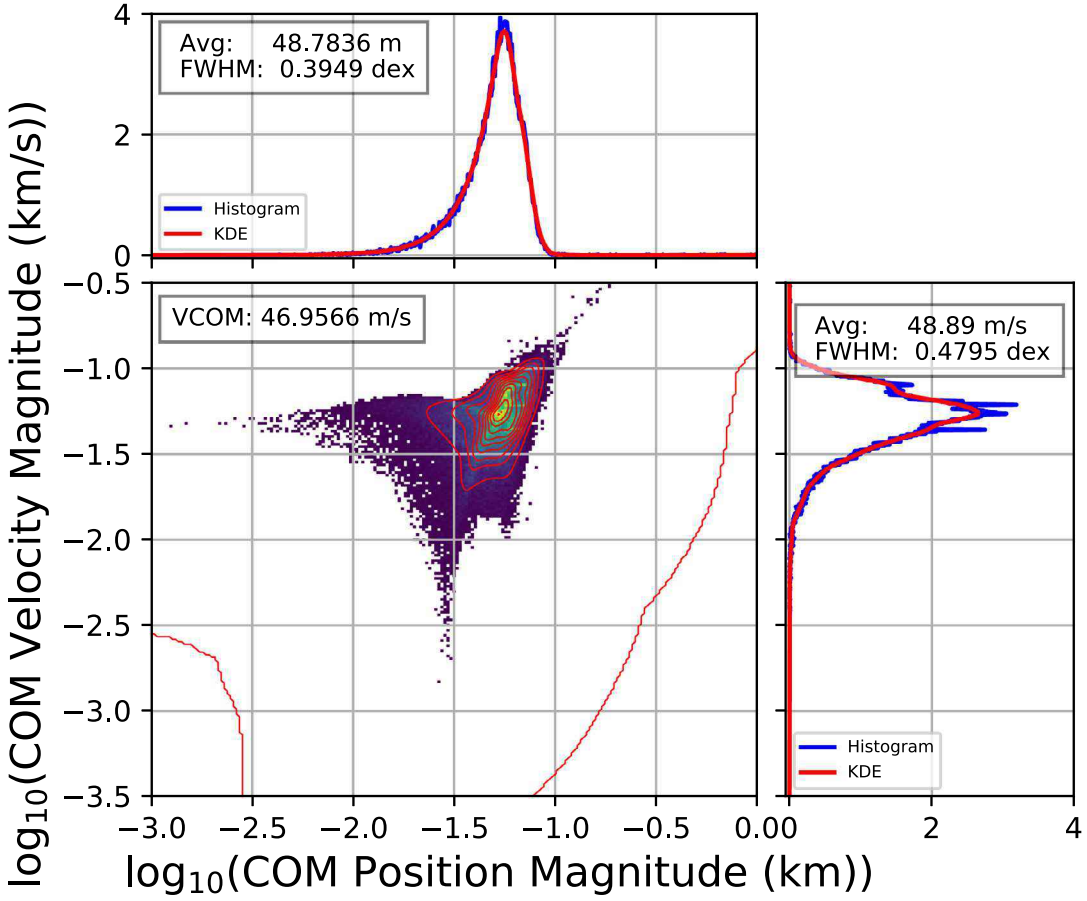

Fig. 2. Histograms and kernel density estimators of position magnitude (top), velocity magnitude (right), and position and velocity magnitude in joint correlation (center) for the fiducial disruption simulation bulk particles in the center-of-mass frame, at 0.5 s in simulation time. Logarithmic scales are used for both position and velocity magnitude. Properties of the distributions and the center-of-mass velocity are annotated.

not expect the catastrophic disruption threshold to be significantly different, it is possible that the physics of standoff nuclear disruption events may change this threshold. However, since the kinetic energy per target mass is so much larger than the threshold reported in [40], we argue that this is a robust disruption, and reaccumulation should be minimal. To demonstrate this further, we compute the average relative velocity between bulk particles that are located within two meters of each other, which estimates the relative velocity of fragment nearest neighbors. The distribution of these relative velocities is plotted in Fig. 3. The geometric average of this relative velocity is 3.2 m/s, which is substantially larger than the estimated escape velocity of the progenitor body (~ 5 cm/s) which further suggests that reaccumulation is negligible, and the disruption is robust.

To study the properties of the disruption, we applied a postprocessing analysis to study the SPH particles in the simulation. Because fragmentation is not modeled in this simulation, we do not capture the exact distribution of fragments expected from this type of disruption event. Instead, we will treat the statistical properties of the SPH particles as a proxy for the fragment properties, with the caveat that the true distributions may be altered by the physics of fragmentation. Nearly all the particles in the energy deposition zones are vaporized and carried away as ejecta/vapor; the bulk particles serve therefore as a proxy for the properties of the fragments. There are some bulk particles that are also entrained in the vapor plume as well, but as a subpopulation should be a small component of the total. The center-of-mass velocity of the bulk particles was computed to be 46.9566 m/s, in a direction 3.053° from the line between the source position and the epicenter on target. The position and velocity magnitudes of the bulk particles in the center-of-mass frame are summarized in Fig. 2. The probability density functions (PDFs) of the velocity and position magnitudes of the particles are estimated using both histograms and a Gaussian kernel density estimator (KDE)[3] in logarithmic space; this is also done in a joint correlation of velocity against position. Here the geometric mean and the (assumed lognormal) full-width at half maximum (FWHM) are annotated for both position and velocity magnitude.[4]

We can carry this analysis further to consider the direction anisotropy of the velocities in the center-of-mass frame. To explore the structure of the expansion of the bulk particles, we computed the spherical harmonic power spectrum[5] of the distribution of the velocity directions of the particles. This power spectrum is plotted in Fig. 3, alongside power spectra corresponding to Gaussian distributions of latitude and longitude on the sphere as proxies for various degrees of pure anisotropy in direction. The Gaussian distributions were computed using the KDE of a sample of randomly generated pairs of latitude and longitude, whose distributions are centered at 0° with $\sigma_{Lon} = 2\sigma_{Lat}$. The power spectra are presented in (root-power) dB relative to the

[3] See e.g. [42] and [43] for a discussion on the use of KDE in estimating PDFs. We use the SCIPY implementation of Gaussian KDE; documentation for SCIPY may be found at http://www.scipy.org.

[4] The lognormal FWHM is given in dex, a quantity equivalent to a Bel that indicates the spread of the distribution of the logarithm of the quantity measured relative to the appropriate unit.

[5] The spherical harmonic power spectrum at l is the sum of the squares of spherical harmonic coefficients of degree l, roughly estimating the contribution to the variance at that degree. We use SHTOOLS, a collection of PYTHON and FORTRAN routines, for computing spherical harmonic power spectra, documented in [44].

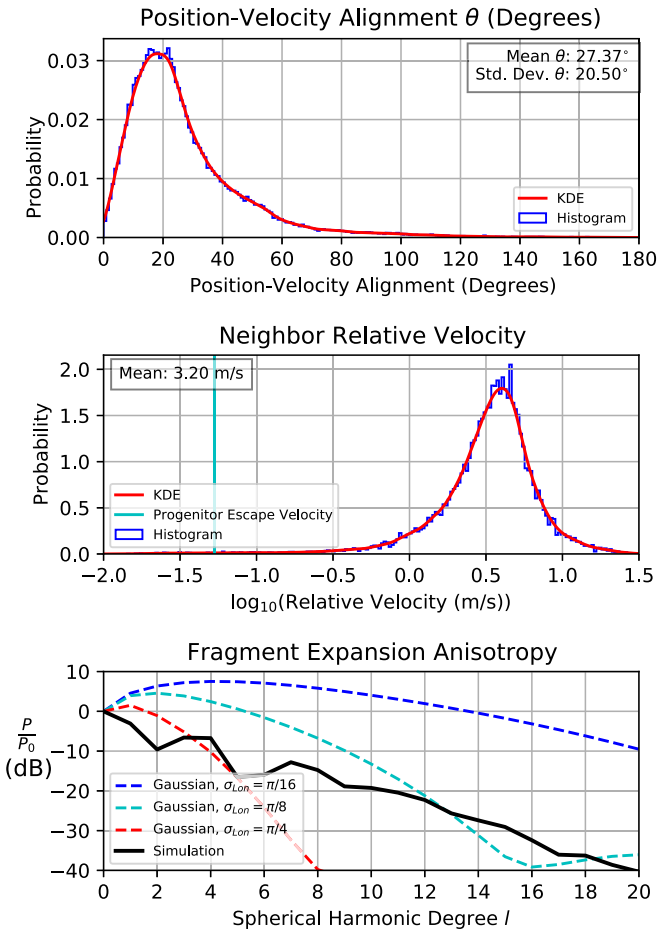

Fig. 3. Diagnostic plots for the nuclear disruption simulation. Top: histogram (blue) and kernel density estimator (red) of the angle θ between the center-of-mass position and velocity vectors of the simulation bulk points, along with annotated mean and standard deviation. Middle: histogram (blue) and kernel density estimator (red) of the distribution of relative velocities of bulk particles in comparison with the neighbors located within 2 meters of each other, compared with the estimated progenitor escape velocity (cyan). Bottom: spherical harmonic power spectrum of the distribution of center-of-mass bulk point velocity longitude and latitude (black), and three Gaussian proxy distributions of varying σ_{Lon}, plotted in (root-power) dB as a function of spherical harmonic degree l. (For interpretation of the references to color in this figure legend, the reader is referred to the web version of this article.)

$l = 0$ power, indicating the relative importance of the higher modes in comparison to the flat ($l = 0$) mode. Unlike the Gaussian proxies, which peak at small but nonzero l modes, the power spectrum of the simulation bulk particle velocity directions peaks at $l = 0$, indicating a primarily flat distribution (though there is some additional structure.) Additionally, we computed the PDF of the angle $\theta = \arccos \frac{\mathbf{r}\cdot\mathbf{v}}{rv}$ between the bulk particle position and velocity to determine how close the simulation velocity distribution is to a purely radial expansion (where $\theta = 0$). This PDF is also presented also in Fig. 3. Though not centered around zero, indicating some non-radial components to the COM velocity, the difference is relatively small (centered around $\sim 20°$).

Taken altogether, the disruption simulation has provided us with an estimate for the center-of-mass deflection component of the fragment velocities (46.9566 m/s), along with an estimate of the typical disruption velocity (geometric mean $\mu_G = 48.89$ m/s) and the width of the disruption velocity distribution ($\sigma_{FWHM} = 0.4795$ dex) that we take to be lognormal. Our studies of the anisotropy of the velocity distribution suggest that it is mostly flat (little direction preference on the whole sphere) and nearly radial (velocities are approximately directed outward in the same direction as their position vector) in the center-of-mass frame. These properties will be used as a prototype for typical disruption scenarios. It should be noted that the properties of the fragment population described here may be significantly altered if the specifics of the nuclear explosive scenario are changed. We do not include other source characteristics such as hard x-rays/gamma rays or neutrons, whose effectiveness is expected to be superior to soft x-rays [13,45]. We also do not self-consistently treat the radiation hydrodynamics of the energy deposition, and the reradiation fraction may vary with incident fluence, or may be a poor approximation at very high fluence. Internal composition and shape variation can also lead to unexpected shock hydrodynamics or radiation transport behavior. For these reasons, we use this model only as a guideline and estimate of disruption performance.

3. Numerical gravitational N-body simulations

3.1. Gravitation in Spheral++

Determining if any fragments created in a disruption event will hit the Earth requires following their orbits to a high degree of accuracy. Previous efforts to study this problem have employed efficient methods built around Keplerian-oriented methods, such as Gauss' planetary equations [17], or the Clohessy–Wiltshire–Hill equations [9,18–20] used in studying spacecraft formations. However, N-body methods have the potential to be more accurate than these approaches, and may reveal effects which are not apparent in the more approximate treatments. This potential comes at the cost of a more computationally expensive treatment and more complicated implementation. We aim to drive the state-of-the-art toward this higher fidelity approach by building a framework around N-body methods as currently supported by Spheral++. We note that while it is not the most efficient approach and that our simulations make tradeoffs in accuracy for efficiency and stability, it is nevertheless an extensible framework that can be improved as new modules and more efficient algorithms are implemented in Spheral++, after which the full strength of our methodology will be realized. Additionally, future three-dimensional simulations of small body fragmentation similar to the one described in Section 2 could be directly placed into Spheral++ N-body simulations for evaluation, once suitably accurate collision operators between fragments are implemented. Our approach is not meant to replace the existing Keplerian-oriented methods, but rather to complement them and to help close out any potential risks in disruption studies by investigating a higher fidelity approach.

The basic framework of these N-body simulations includes the major large bodies[6] in the solar system as a means to construct a reasonable and realistic gravitational model, which manifestly includes planetary interactions as a bonus. This approach was favored over alternatives such as disturbing functions as this treatment is a simple and natural use of particle representation in Spheral++. Each large body is placed in the N-body simulation as single massive particles, using suitably chosen Cartesian state vectors (position and velocity) for each large body (see Section 3.5 below): we make no attempt to include tidal interaction terms and treat them purely as point particles. Additionally, we do not include any solar wind or radiation interaction terms, whose effects should be small on the short timescales we consider in this work. As a final initial condition, the well-separated fragment field (see Section 3.4) is placed with its center-of-mass on a realistic Earth impact orbit (see Section 3.2) and integrated forward, taking care to ensure that the force calculation accuracy is maintained to a desired tolerance.

The Spheral++ N-body gravity module currently supports either particle–particle N-body gravity, which is $\mathcal{O}(N^2)$ runtime in particle number, and oct-tree gravity based on the Barnes–Hut method, which

[6] Here, *large bodies* refer to the Sun, the planets, and the Moon, with Neptune omitted if sufficiently accurate ephemerides are not available.

can achieve $\mathcal{O}(N \log N)$ runtime in particle number [46,47]. The oct-tree gravity, by reducing the expense of computing the force due to closely spaced particles at large distances, can improve simulation performance, depending on the separation of particles. However, since the fragment fields should remain relatively closely spaced relative to the scale of the solar system, the Barnes–Hut method will not provide a significant increase in algorithmic efficiency, and the computation time is dominated by the fragment–fragment forces. Nevertheless, we choose this method, with opening parameter[7] $\theta = 0.5$, for this work, as there is a minor improvement in efficiency between the large body-fragment force calculation, and we have found that there is no practical loss of accuracy compared to the full N-body method. We note that algorithms, such as a kd-tree method of the type used by the PKDGRAV [48] code, may offer further improvements in efficiency, which we will explore in future work. Pairwise gravitational forces in SPHERAL++ are softened according to the standard softening scheme due to Aarseth [49]:

$$\mathbf{F}_{ij} = -\frac{Gm_i m_j}{r_{ij}^2 + \varepsilon^2}\hat{\mathbf{r}}_{ij}, \tag{5}$$

where $\mathbf{r}_{ij}$ is the pairwise separation vector (specifically, $\mathbf{r}_{ij} = \mathbf{r}_i - \mathbf{r}_j = -\mathbf{r}_{ji}$) and ε is the softening length, which is used to ensure integrator stability and soften the effects of close encounters. Softening is desired, despite its detrimental effects on accuracy, to screen any close encounters in the system.[8] This form provides a simple form for the relative error in the softened gravitational force at a given separation distance r:

$$f(r) = \left|\frac{\Delta F}{F}\right| = \frac{\varepsilon^2}{r^2 + \varepsilon^2}, \tag{6}$$

With the exception of the impactor or the fragments, the typical smallest expected separation between the large bodies of our system is the Earth–Moon distance. A convenient choice for the softening length in our system (which in this case is referred to as the far-field softening length, to distinguish from the near-field softening length which we discuss below in Section 3.3) is

$$\varepsilon_{FF} = 0.5 R_{\oplus}, \tag{7}$$

which results in force calculation errors at the Earth–Moon distance of roughly $f = 7.7 \times 10^{-5}$, but nevertheless has relatively good timestep performance. This error may be relatively high for long solar system integrations, but for short timescales relevant to planetary defense this is acceptable; we discuss drift in our simulations in more detail in Section 3.6. This permits rapid calculation, with serial runtimes on the order of a few hours, permitting a wide exploration of parameter space. This trade-off is satisfactory for the majority of our calculation, except when the impactor or fragments approach the Earth or other solar system bodies (discussed in Section 3.3) or for the force calculation between the closely spaced fragments (discussed in Section 3.4.)

We use a second-order Verlet (kick–drift–kick leapfrog) integrator of the type described in [23], implemented in SPHERAL++. This integrator has many excellent properties, including second-order accuracy, time-reversal symmetry, and symplecticity (see e.g. [50]) in the absence of dissipation, while remaining inexpensive computationally, though our choices in simulation strategy do destroy exact time-reversal symmetry. More details about our integrator choice are presented in Section 3.6.[9]

We note that we are focusing on short times-to-impact in this work, and so accumulated errors from our simulation scheme can be kept to a minimum. We allow the global timestep of the simulation to vary using a commonly employed criterion used with softened gravity (see, e.g. [51]), which allows us to define a timestep relative to the softening scale of the system:

$$\Delta t \propto \sqrt{\frac{\varepsilon}{|\mathbf{a}_{max}|}}, \tag{8}$$

where $|\mathbf{a}_{max}|$ is the maximum acceleration magnitude of particles in the simulation. Softening will bound the particle acceleration, and therefore the timestep should be at minimum $\propto \varepsilon^{3/2}$, i.e. a larger softening length enables a simulation to tolerate larger timesteps. Specifically, our simulations typically achieve $\sim 10^3$ seconds/timestep when the far-field softening length is employed, and decreases to ~ 10 seconds/timestep when the near-field softening length is used instead.

Taken altogether, the simulation schematic is given below.[10] The details in these steps are explained in the remaining subsections. Generally, the simulation will take the desired orbital characteristics, the date of impact, and the time to impact that are desired to be simulated as inputs and determine the appropriate initial state of the system, especially the impactor position and velocity, using a time-reversal approach outlined in Section 3.2. The fragment field is then initialized at those initial conditions, with desired deflection and disruption characteristics, and integrated forward in time; impacting fragments are detected and removed from the simulation. This approach is broken into different phases to ensure that different effects are captured appropriately.

- *Phase 1*: First initialize the impactor and large bodies (without the Earth and Moon) with the appropriate Cartesian state vectors at the time of impact; reverse the sign of the velocities; and integrate backwards using the near-field softening length by a time equal to Δt_{Dekick}, whose selection is outlined in Section 3.3. This is done to prevent a close encounter between the Earth and the impactor before we integrate it backwards.
- *Phase 2*: Next initialize only the large bodies (including the Earth and Moon), and again integrate backwards in time (using the near-field softening length) by the same amount in the first phase. This provides the Earth and Moon state vectors after Phase 1.
- *Phase 3*: Then, place the large bodies and impactor from Phase 1, and the Earth and Moon positions and velocities from Phase 2, and continue to integrate the now complete system backwards in time (but using the far-field softening length) to the desired time of the disruption event, less the (relatively small) expansion time of the fragments during the self-gravity phase. The simulations are cached after the completion of this Phase to avoid recalculating Phases 1 through 3 repeatedly.
- *Phase 4*: Next, using the positions and velocities from Phase 3, replace the impactor with the appropriate expanded fragment field, and integrate the system forward (using the far-field softening length) until the reference orbit reaches the point at which the distance between the reference orbit and the Earth is small enough that the gravitational force error due to the far-field softening length is too large according to our tolerance.
- *Phase 5*: Last, integrate the system forward using the near-field softening length until at least the projected impact time. In practice, we integrate slightly further to ensure that any fragments whose orbits were slightly retarded but would nevertheless still result in an impact are included in the impact fraction.

[7] This parameter is a threshold for determining when to approximate the gravitational force from a tree cell; it is usually set to less than $1/\sqrt{3} \sim 0.57$ for accuracy; we have opted for a relatively large value to maximize the modest improvement in efficiency. See e.g. [47].

[8] Any true close encounter will be captured provided that the softening length is less than the physical extent of the particles in the system, though the force will not be correct due to softening. Any encounter at a smaller radius would, in fact, result in an impact.

[9] We intend to implement higher-order alternatives, such as Burlisch–Stoer or mixed-variable symplectic integrators, in future work.

[10] Orbit verification may be achieved by simply integrating the impactor forward without replacing it with a fragment field. Each scenario was tested to ensure impacts occurred reliably. Additionally, pure deflection is easily modeled in our system by simply adding a single deflection velocity to the impactor.

If the desired time-to-impact is very short (shorter than the time necessary to traverse the near-field simulation region) then the simulation will automatically skip Phases 3 and 4, and substitute the fragment field for the impactor at the beginning of Phase 5.

3.2. Hazardous orbit selection

The gravitational influence of the planets perturbs the two-body orbital elements of small bodies away from their average values at any osculating point measurement in the small body's orbit. Over time, these changes can accumulate, and in the case of close encounters, can kick the body into a new set of orbital parameters. For this reason, it is nontrivial to choose appropriate Cartesian state vectors in the reference frame of our simulation for the impactor that will appropriately preserve the desired orbital characteristics throughout its orbit prior to the impact with the Earth, from a forward-modeling standpoint. This difficulty cannot be avoided except in very short times-to-impact, in which the impactor is very close to the Earth and the overall influence of other bodies in the system is small; it is also unavoidable even in Keplerian-type approaches if other large bodies are present in the system to some degree. Indeed, this difficulty has been recognized in [19], in which an adaptive shooting method is presented to solve this problem in their eccentric Clohessy–Wiltshire–Hill system augmented by fragment–fragment gravity. To solve this issue, we will exploit the approximate time-symmetry of the Verlet leapfrog integrator in the Spheral++ N-body gravity calculations (see Section 3.1) to determine an appropriate set of state vectors for our impactor prior to disruption, which includes the perturbing influence of the major bodies in the solar system. This is done by first integrating the system reverse in time from the point of impact back to the appropriate time we desire to simulate, which provides the initial conditions for all bodies in the forward simulation, with the exception of the impactor, which is replaced with an appropriate fragment field. This approach neatly captures the aggregate influence of the whole N-body system on the orbit while maintaining the desired orbital characteristics of the unperturbed impactor and manifestly results in an impact when the impactor is integrated forward in time. Each scenario considered in this work was individually checked to ensure that impacts occur if no action is taken.

We will restrict our analysis to only elliptic orbits, though this procedure could be extended to hyperbolic orbits in principle. The first task is to determine the Cartesian velocity vector at the point of impact which results in an (unperturbed) two-body orbit with the selected orbital characteristics: semimajor axis a_{imp}, eccentricity e_{imp}, and inclination i_{imp}. (The underlying physics is presented in Ch. 2 of [52].) Additionally, since the impactor and the Earth will share the same focus (the Sun), there are two nodes at which impact can occur, and therefore one must choose whether the impactor approaches from the day side (interior to the Earth's orbit, moving outward) or the night side (exterior to the Earth's orbit, moving inward.) Using the standard gravitational parameter $\mu = GM_\odot$, we adopt the nondimensionalization for velocity $\mathbf{v}$:

$$\mathbf{V} = \sqrt{\frac{a_{imp}}{\mu}}\mathbf{v} \tag{9}$$

and the natural nondimensionalization for position $\mathbf{r}$:

$$\mathbf{R} = \frac{\mathbf{r}}{a_{imp}}. \tag{10}$$

The vis-viva equation can be used as one constraint on the components of $\mathbf{V}$:

$$V^2 = V_x^2 + V_y^2 + V_z^2 = \frac{2}{R} - 1. \tag{11}$$

Using the orbital angular momentum and the inclination angle, it is possible to obtain two more constraints, one for the z component of the angular momentum and another from the magnitude of the angular momentum:

$$R_xV_y - R_yV_x = \sqrt{1-e_{imp}^2}\cos i_{imp}, \tag{12}$$

$$\left(R_yV_z - R_zV_y\right)^2 + \left(R_xV_z - R_zV_x\right)^2 = \left(1-e_{imp}^2\right)\sin^2 i_{imp}. \tag{13}$$

These three constraints (and day/night side approach choice) are sufficient to find a unique $\mathbf{V}$. In practice, we use the SciPy [53] optimization and root-finding package to solve this system, cast as a vector root finding problem. Specifically, we used the multidimensional `scipy.optimize.root` function, with two choices for method: the `lm` method, which uses a modified version of the Levenberg–Marquardt algorithm to solve the equations in a least squares sense; and the `hybr` method, the MINPACK implementation of the hybrid Powell method [53]. These methods were generally found to converge rapidly to very high accuracy, but for some parameter choices the solution failed to converge to an acceptable solution. Accordingly we evaluate both of these solution methods for each parameter set and choose the method that yields the best solution, judged as reproducing the desired parameters. Both of these methods require choosing an appropriate initial guess so that the root finding algorithm converges. We can formulate such a guess by using cross product rules and the angular momentum vector, $\mathbf{h} = \mathbf{r}\times\mathbf{v}$:

$$\mathbf{v} = \left(\frac{\mathbf{r}\cdot\mathbf{v}}{r}\right)\left(\frac{\mathbf{r}}{r}\right) - \frac{\mathbf{r}\times\mathbf{h}}{r^2}. \tag{14}$$

While the first term is not identically zero, we can expect it to be fairly small, so we can begin to formulate our guess using only the second term. The magnitude of the angular momentum is given by $h^2 = \mu a_{imp}(1-e_{imp}^2)$, so we let our initial guess $\tilde{\mathbf{V}}$ in nondimensionalized variables be

$$\tilde{\mathbf{V}} = -R^{-2}\sqrt{1-e_{imp}^2}\left(\mathbf{R}\times\tilde{\mathbf{H}}\right) \tag{15}$$

where $\tilde{\mathbf{H}}$ is a reasonable guess for the angular momentum unit vector. In terms of orbital elements, $\mathbf{H}$ should be [52]:

$$\mathbf{H} = \begin{pmatrix} \sin\Omega\sin i_{imp}\ \operatorname{sign}\left(\cos i_{imp}\right) \\ -\cos\Omega\sin i_{imp}\ \operatorname{sign}\left(\cos i_{imp}\right) \\ \cos i_{imp} \end{pmatrix}, \tag{16}$$

where Ω is the longitude of the ascending node corresponding to the position $\mathbf{R}$. Since the Earth has a small inclination, we could expect this to be approximately just the position angle of the x and y components of the Earth's position at impact within the Earth's ecliptic, so our choice for $\tilde{\mathbf{H}}$ is

$$\tilde{\mathbf{H}} = \begin{pmatrix} \frac{y}{r}\sin i_{imp} \\ \frac{x}{r}\sin i_{imp} \\ \cos i_{imp} \end{pmatrix}. \tag{17}$$

We can improve this guess further by returning to the term we dropped and providing a reasonable estimate. In terms of the angle θ between $\mathbf{r}$ and $\mathbf{v}$, this term is

$$\left(\frac{\mathbf{r}\cdot\mathbf{v}}{r}\right)\left(\frac{\mathbf{r}}{r}\right) = v\cos\theta\left(\frac{\mathbf{r}}{r}\right). \tag{18}$$

One can easily obtain v from Eq. (11), but $\cos\theta$ does not have a simple expression. Nevertheless, it is clear that this term vanishes for a circular orbit, so $\cos\theta = 0$ when $e_{imp} = 0$; as the eccentricity increases, the angle between them should grow smaller (and so $\cos\theta$ increases.) A simple choice is to adopt the approximation $\cos\theta \sim e_{imp}$. Here is also an appropriate time to introduce the day side/night side approach choice mentioned above, as the sign of $\mathbf{r}\cdot\mathbf{v}$ indicates the approach choice:

$$\mathbf{r}\cdot\mathbf{v} \geq 0 \quad\Rightarrow\quad \cos\theta \geq 0, \qquad \text{(day side)} \tag{19}$$

$$\mathbf{r}\cdot\mathbf{v} \leq 0 \quad\Rightarrow\quad \cos\theta \leq 0. \qquad \text{(night side)} \tag{20}$$

Adopting this and combining with our previous guess gives our final form for the velocity estimate:

$$\tilde{\mathbf{V}} = R^{-1}e_{imp}\left(\frac{2}{R} - 1\right)\mathbf{R} - R^{-2}\sqrt{1-e_{imp}^2}\left(\mathbf{R}\times\tilde{\mathbf{H}}\right) \tag{21}$$

Practically, to ensure the solution converges to the correct approach choice, we add a penalty to each constraint equation that is zero when Eq. (19) or (20) is satisfied and a large number otherwise.

To test our implementation, we chose to explore many choices of parameters and ensure that the numerical errors in both the constraints (Eqs. (11),(12),(13)) is low and that the orbital parameters (as determined from our computed Cartesian state vectors) are indeed the ones we chose. To that end, we tested our method using 250 choices each of a_{imp}, e_{imp}, and i_{imp}, and considering both day side and night side approaches, spanning likely values for hazardous asteroids. It is important to ensure that the desired orbit is physically realizable, i.e. that the final position magnitude lies between the perihelion and aphelion of the orbit specified:

$$a_{imp}(1 - e_{imp}) \leq r \leq a_{imp}(1 + e_{imp}). \tag{22}$$

This provides a minimum semimajor axis bound for impactors with elliptic orbits, as the maximum eccentricity is 1, so the semimajor axis must be at least $r/2$. For other semimajor axis values less than r, it is simple to see that the minimum eccentricity must be $\frac{r}{a_{imp}} - 1$; similarly, for semimajor axes greater than r, the appropriate criterion is $1 - \frac{r}{a_{imp}}$. We exclude parameter choices that fail this criterion. We chose to explore semimajor axes ranging from the minimum (roughly 0.5 AU) to 5.5 AU, a rough estimate that includes most nearby asteroids in the solar system, including Jupiter Trojans and Greeks. Because of the slight inclination of the Earth's orbit, it is not possible for a zero inclination orbit to successfully hit the Earth except for the two Earth orbit nodes, so we explore inclinations lying between 1 and 179 degrees. Finally, to span all elliptic orbits, we explore eccentricities ranging from zero to 0.999 (to exclude parabolic orbits.) The total squared error in the constraint equations, and the squared error between chosen and derived a_{imp}, e_{imp}, and i_{imp}, is plotted in Fig. 4 versus eccentricity and semimajor axis, where the error is then summed over all inclination angle choices. The total accumulated error is quite small for most orbits, being of the order of 10^{-14}. There are some choices that nevertheless fail (the bright points in Fig. 4); for this reason, even though this method works for the vast majority of possible parameter choices, each choice should be individually checked to ensure the root-finding routine converged correctly. Each scenario considered here was tested to ensure that this time-reversal, rootfinding procedure results in systems that, when integrated forward, achieve Earth impacts reliably.

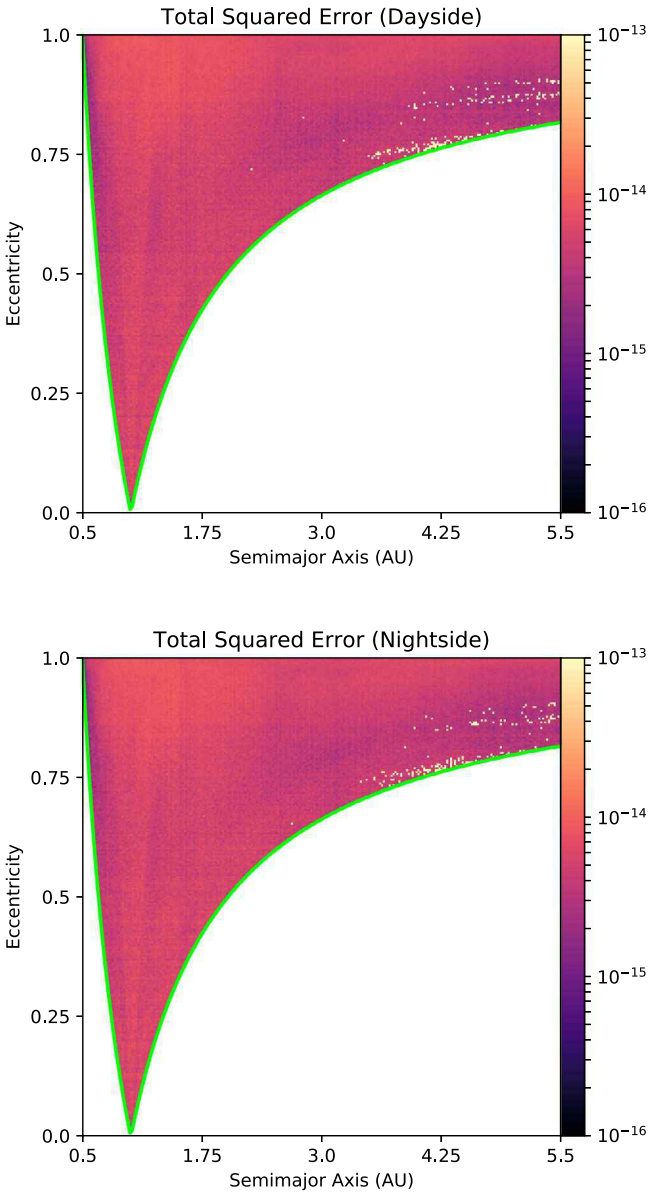

Fig. 4. Total squared error in the solutions to the constraint equations ((11), (12), (13)), added to the total squared error in the orbital parameters (a_{imp}, e_{imp}, I_{imp}) summed over all inclination angles. The annotated green line delineates the minimum eccentricity for each semimajor axis as defined in Eq. (22). (For interpretation of the references to color in this figure legend, the reader is referred to the web version of this article.)

3.3. Dekick distance and gravitational focusing

The aforementioned perturbing influence of the other large bodies in the solar system leads to accumulated changes in the osculating orbital parameters of the impactor, which is nevertheless captured in our simulation scheme. However, our method places the impactor initially on a close orbital encounter with the Earth. The resulting gravitational kick is usually sufficient to put the impactor on a new set of orbital parameters that differ from those used to select the hazardous orbit in Section 3.2. For this reason, we first integrate the orbit backwards in a system without the Earth–Moon system in place for a short period of time so that the body is not subject to this initial kick, sufficient to traverse a distance we call the *dekick distance*. This must be balanced against integrating too far without the influence of the Earth–Moon gravity, as one of the virtues of our approach is that the orbit results in an impact by construction. This approach also includes the gravitational influences of all bodies we place in the simulation on their natural orbits with correct relative orbit timing, while retaining nearly the same orbital parameters that we chose initially. A natural choice is set the dekick distance to the radius of the Earth's Hill sphere, R_{Hill}, which defines the volume of space in which the Earth's gravitational influence exceeds the Sun's; this ensures that the perturbing influence of the Earth is bounded.

Another problem occurs when the simulation returns to the impact time, in which the fragments enter the Earth's Hill sphere and are strongly affected by its gravity. Gravitational focusing [54,55] is expected to raise the effective cross-section of the Earth to the fragments on their encounter orbit with the Earth, and so including this effect is critical for accurately determining impact risks. This enhancement of the true cross section relative to geometric is

$$\frac{\sigma}{\sigma_{geo}} = 1 + \frac{v_{esc}^2}{v_{rel}^2}, \tag{23}$$

where v_{esc} is the Earth's escape velocity and v_{rel} is the relative velocity of the fragment and the Earth prior to the encounter. Since impact velocities (and hence relative velocities) are of the order of tens of km/s, and the Earth's escape velocity is about 11.2 km/s, this effect can be significant. Nevertheless, for time-stepping performance, it is necessary to set the softening length to a relatively large value during the majority of the simulation, when the gravitational force error due

to softening is very low (see Section 3.1.) As a result it is necessary for us to halt our simulation once the gravitational force error becomes intolerable, and proceed using a new softening length (which we call the near-field softening length in contrast to the far-field softening length described in Section 3.1) that is sufficiently small in order to capture gravitational focusing. The relative error (see Eq. (6)) at the Earth's Hill radius using the far-field softening length is roughly $f(R_{Hill}) = 4.7 \times 10^{-6}$, making that a convenient choice to address this problem by pausing the calculation when the reference orbit[11] reaches that distance from the Earth. This also ensures commonality with the reverse-time calculation close encounter correction described above, which should help maintain approximate time-symmetry. To ensure the accuracy of the force calculation for gravitational focusing, we choose a near-field softening length such that the force error at one Earth radius is $f(R_\oplus) = 10^{-5}$; in terms of Earth radii, our near-field softening length satisfying this constraint is roughly

$$\varepsilon_{NF} = 0.003 R_\oplus \tag{24}$$

In both of these scenarios, it is necessary to determine the Earth-impactor distance at short times before impact, which will vary depending on the orbital parameters of the impactor. This is a nonlinear problem. However, for relatively short times and therefore small changes in the eccentric anomaly of the impactor, relatively high accuracy is maintained by the third-order approximant obtained by truncating the series expansion in δE, whose calculation is outlined in Appendix. Thus the determination of the desired integration time, as a function of impactor orbital parameters, can be computed by simply selecting the positive root of the resulting cubic. This procedure ensures the preservation of desired orbital parameters and the accuracy of gravitational focusing for arbitrarily selected orbits. To ensure that no fragments are within the Hill sphere of the Earth, we choose the Earth-impactor distance at which we switch integrators to be twice the Hill radius.

Because of both the required integration phase to traverse the dekick distance and the gravitational focusing in the forward orbits, precise impact localization is challenging. Since we are focusing on a basic risk assessment using hypothetical scenarios, we have not implemented this capability, but our simulations will capture the general behavior of the disruption, especially the impact fraction. Such a capability will need to estimate the correction to the initial Cartesian state vectors necessary to offset gravitational focusing deflection from the desired impact point, and may need to incorporate other higher-order effects if high precision is desired.

3.4. Fragment initial conditions and fragment self-gravity

Following a disruption event, the progenitor body is broken into many fragments of varying mass, each of which has a unique position and velocity relative to a frame centered on the original progenitor. This process proceeds over timescales quite rapid relative to orbital dynamics (on the order of minutes at most), sufficient to be virtually instantaneous. The fragment state vectors in the disruption frame serve as the initial conditions of the forward orbit integration described in Section 3.1. They are placed with their center-of-mass on a selected realistic Earth impact orbit (see Section 3.2 above), and their Cartesian velocity vectors are augmented with the post-disruption velocities.[12]

For simplicity, we will adopt a simple two-velocity parametric form for the post-disruption velocities: one center-of-mass deflection component (whose direction is adjustable in accord with controllable mission parameters) and the individual fragment disruption velocity in the center-of-mass frame, which is directed radially outward according to the fragment position:

$$\mathbf{v}_i = \mathbf{v}_{def} + v_{dis,i}\hat{\mathbf{r}}. \tag{25}$$

Here we have included an index for v_{dis} to indicate that each fragment may have an individual choice sampled from a distribution of disruption velocities, such as one informed by the disruption velocity distribution presented in Section 2.2.

Relative position uncertainty of even kilometers correspond to timing uncertainty on the order of at most minutes, and so the position accuracy of the fragments is less important to the resulting orbit. The relative importance of the velocity distribution has been acknowledged in previous work; in [17], the position probability distribution was chosen to be a (vector) delta function, and much of their modeling focused on the velocity distribution. More extensive fragmentation modeling will provide mass, velocity, and position distributions for the fragments that are consistent in their joint probabilities. In Section 2.2, the velocity distribution in the center-of-mass frame was found to be nearly flat and radial, and that a spherically symmetric distribution of fragment directions is sufficient for our modeling purposes, whose direction and position is fixed but whose velocity is allowed to vary. This approximation is equivalent to assuming the fragments follow a nearly ideal spherically-symmetric expansion in the instantaneous center-of-mass frame. To generate such a distribution of directions for N fragments, we employ a parameterized spiral scheme, identical to the one described in [56] and discussed in [57]. This parameterization uses a stepping parameter to determine the kth polar and azimuthal angles:

$$h_k = -1 + \frac{2(k+1)}{(N-1)}, \quad 1 \le k \le N,$$

$$\theta_k = \arccos h_k, \tag{26}$$

$$\phi_k = \phi_{k-1} + \frac{3.8}{\sqrt{N}\sqrt{1-h_k^2}},$$

with $\phi_0 = \phi_N = 0$. This scheme provides a fast realization for a roughly equal, optimized area packing partition of the sphere surface for N particles, which allows our fragment field to sample different radial directions evenly. (See [57] for applications of this scheme to other problems in SPH.)

For reasonable time-stepping performance and integrator stability, the softening length of the simulation is set too large to accurately capture the effects of self-gravity on the evolving fragment field for some time following disruption, even for the near-field softening length described in Section 3.3. Indeed, the close proximity of the fragments is the principal reason we have adopted softening in the first place. Without an accurate collisional interaction operator between fragments, any system with significant reaccumulation will result in an unstable system of close encounters that will, at best, have very poor time-step performance. Provided that the disruption velocity for a fragment is above the escape velocity of the body at its surface, it can be reasonably assumed that this particular fragment has become unbounded, which is true in the case that a single small fragment is being ejected from a larger monolithic body. However, in catastrophic disruption scenarios, the assumption in calculating the escape velocity is no longer valid, as the gravitational potential is no longer approximately static. The near field evolution of the fragment field under the influence of its own gravity is a subject demanding more than the scope of this work, but we will adopt a simplifying assumption that any fragment whose disruption velocity is sufficiently low will automatically reaccumulate. Assuming

[11] While the fragments may be closer to Earth relative to the reference orbit at this calculation time, this distance will not be large enough to introduce a large degree of force calculation error provided a small enough tolerance is chosen.

[12] Methods such as Gauss' planetary equations could be used to determine the relative orbital parameter changes for each fragment subject to a velocity change, but our simulation approach works in the Cartesian frame without requiring an individual orbital element description for each fragment. Additionally, these equations do not naturally include the many-body gravitational effects in the system.

Table 2
Hypothetical impact scenario parameters for each scenario chosen in our study: semimajor axis a, eccentricity e, inclination i, dayside/nightside node approach, and mean motion n.

Scenario	Object Name	Impact Date	a (AU)	e	i	Approach	n (yr^{-1})
P	PDC 2019	2027-Apr-27	1.915	0.5352	18.0°	Nightside	2.37
A	99942 Apophis	2029-Apr-13	0.922	0.1912	3.33°	Nightside	7.09
B	101955 Bennu	2060-Sep-23	1.126	0.2038	6.03°	Nightside	5.26
C	(343158) 2009 HC_{82}	2080-Dec-30	2.527	0.8069	154°	Nightside	1.56
D	(5496) 1973 NA	2030-Jun-23	2.435	0.6359	68.0°	Dayside	1.65

a spherical body with radius R and average bulk density ρ, the escape velocity scales:

$$v_{esc} = 1.057 \text{ m/s} \left(\frac{\rho}{2 \text{ g/cc}}\right)^{1/2} \left(\frac{R}{1 \text{ km}}\right) \tag{27}$$

All reaccumulated fragments will instead be treated as a single fragment with $v_{dis} = 0$ (i.e. a pure deflection.) This seems sensible as reaccumulation should proceed at the dynamical timescale $\tau \simeq \sqrt{1/G\rho} \sim 45$ minutes for our fiducial density, which is much shorter than our orbit integration times. For the unbound fragments, we will assume that the disruption velocity will be reduced by the gravitational binding energy of the body:

$$U_{GB} = C_G \frac{GM^2}{R} \tag{28}$$

where C_G is a constant depending on the exact shape and density profile of the body; for a uniform sphere, $C_G = 3/5$. A simple energy balance argument provides:

$$v'^2_{dis} = v^2_{dis} - \frac{C_G}{2} v^2_{esc}. \tag{29}$$

This will not treat the fragment self-gravity exactly, but should provide a reasonable estimate of its effects. Our simulations allow C_G to be chosen arbitrarily, but a nominal $C_G = 3/5$ will be adopted in this work. Comparisons against an exact treatment are postponed to a future study. We will fix the radius of all the fragments to be 1 km from the center of the fragment field located at the reference impactor orbit, which introduces a minor error on the order of a few seconds in the exact timing of the disruption event. We are free to assume the intervention occurred slightly earlier than exactly the time specified without affecting the physics of the system, and relative to the typical orbit integration time (on the order of months) the difference is negligible.

We note that the N-body approach outlined here, given that we are softening out the fragment–fragment interactions, may be criticized on the grounds that the dominant computational expense is expended on the fragment–fragment forces. However, the general framework is not dependent on the relatively large softening length we employ. One means to mitigate this issue is to add another simulation Phase between Phase 3 and 4 that integrates the fragments without softening to properly capture their self-gravity. Nevertheless, when the disruption is robust, the self-gravity effects are weak compared to the more important large body effects, especially gravitational focusing. For this reason, we do not include this extra simulation Phase in this work. Moreover, our simulations do not unduly suffer from the computational expense incurred by the N-body approach: each study discussed in Section 4 can be completed in less than 24 h of runtime with only relatively modest computing requirements. Our use of a relatively large softening length that softens out the fragment–fragment forces is responsible for this performance, which should be regarded as a simulation tradeoff. Lastly, we note that while the *initial* interactions between fragments are softened out, as the fragment field separates the softened fragment–fragment force calculations become progressively more accurate. Future studies involving more marginal disruptions, especially once collision operators are implemented, will benefit from these methods.

It should also be noted that this idealization of both the velocity and position distributions fails to capture many effects that could become very important in a realistic risk assessment. Besides orbital timing errors and overestimation of self-gravity effects, if there is a preference in certain directions for more fragments (or higher mass fragments) then the impact risk will be concentrated in some directions and diluted in others; this goes similarly to any preferential direction (in the center-of-mass frame) with greater disruption velocities. Future efforts that fully capture the fragment distributions of mass, position, and velocity that are consistent in a joint probability sense (whose correlations are known and sampled from accordingly) as well as treating the near-field self-gravity evolution of the fragments will permit our simulation scheme to achieve greater fidelity, and we also note that such schemes are straightforward to implement using our methodology. However, because we have adopted our simplified scheme, these efforts must be regarded as risk assessment estimates which capture broad behavior but cannot provide absolute, calibrated guarantees against impacts.

3.5. Hypothetical impact scenarios

To provide the most accurate gravitational environment within which to study the orbits of the fragment field, our system should include the influence of the major bodies of the solar system in addition to the Sun, despite the Sun's obvious gravitational dominance in nearly all regions of the solar system. Crucially, the influence on the planets (notably Jupiter) on the Cartesian state vectors of the Sun should not be neglected in a high-fidelity model. We employ the NASA JPL HORIZONS database[13] to obtain these state vectors for a chosen impact time, which will depend on the specific scenario modeled. For each body there is a finite length of time into the future that the HORIZONS database can provide accurate state vectors, due to unavoidable errors in prediction that accumulate over time. For scenarios where this is the case, the large bodies for which this is the case are omitted from the system.

The selection of an impact scenario requires the specification of three orbital parameters (semimajor axis a, eccentricity e, and inclination i); the time of impact; and choice of the two possible intersection points (see Section 3.2 for more details.) We shall consider five different impact scenarios for our study: the 2019 Planetary Defense Conference hypothetical impact scenario[14]; a modification of the close approach of 99942 Apophis on April 13, 2029; a modification of the close approach of 101955 Bennu on Sept. 23, 2060; a modification of the close approach of (343158) 2009 HC_{82} December 30, 2080; and a modification of the close approach of (5496) 1973 NA on June 23, 2030.[15] The hypothetical impact scenario parameters are presented in Table 2.

The PDC 2019 hypothetical impact scenario is chosen for direct relevance to any results presented and exercises conducted during the

[13] The HORIZONS online ephemeris system is available at http://ssd.jpl.nasa.gov/?horizons.

[14] Details about the scenario may be found at https://cneos.jpl.nasa.gov/pd/cs/pdc19/.

[15] These scenarios were selected using the NASA/JPL Small Bodies Database, available at https://ssd.jpl.nasa.gov/sbdb.cgi. For each scenario (except PDC 2019), the date of close approach is selected as the time of impact (setting the time to 00:00:00.0000 Barycentric Dynamical Time) and the orbital elements selected to match those of the selected body, which will result in an orbit similar to the actual body but constructed to result in an Earth impact at the specified time.

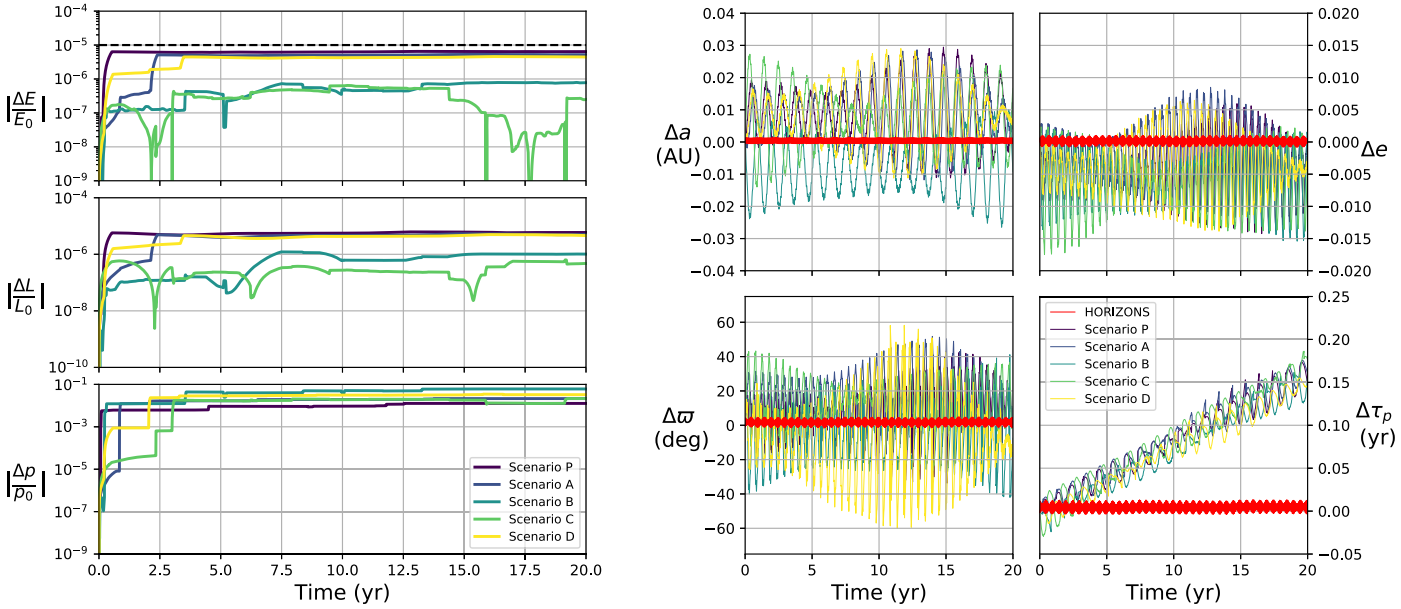

Fig. 5. Estimates of drift in our simulation accuracy versus time difference from the final Earth impact state. The final state is at zero years; positive time denotes time before the final state, so Phase 3 integrates from zero to twenty years, while Phase 4 integrates from twenty to zero years. Left panel: drift in the integrals of the motion measured during the long orbital integration phases (Phases 3 and 4) for accuracy assessment. The energy, angular momentum, and linear momentum are presented relative to the initial values in this phase of the simulation for each scenario described in Section 3.5. Time symmetry is maintained, so each plot is identical after time reversal; both Phases are plotted but are indistinguishable at identical system states. In the right panel, the drift in the Earth's osculating semimajor axis a, eccentricity e, argument of pericenter ϖ, and time of pericenter passage τ_P are presented relative to the corresponding values in the JPL HORIZONS database at the appropriate time. For comparison, the relative drift in the JPL HORIZONS osculating orbital parameters for the Scenario P dates are presented in red. (For interpretation of the references to color in this figure legend, the reader is referred to the web version of this article.)

2019 Planetary Defense Conference. 99942 Apophis and 101955 Bennu were chosen due to their prominent close approaches and the wealth of studies focused on them in past and future missions. (343158) 2009 HC_{82} has a retrograde orbit and was once the object with the highest known relative velocity (about 63 km/s) that passed within 0.5 AU of Earth, making this case an interesting extreme scenario. (5496) 1973 NA was, at one point, the most highly-inclined minor planet known, and had a relatively close approach (less than 0.08 AU) on July 2, 1973; it has both high inclination and would result in an impact on a dayside node. These scenarios provide a reasonable range of possible (but realistic) orbital parameters for impact risk assessment. For brevity each scenario is labeled by a letter indicated in Table 2.

3.6. Range of validity and errors in the N-body simulations

Though we use a second-order accurate and time-reversible integrator, there are nevertheless unavoidable errors associated with numerical integration of an N-body system that may become significant. Additionally, variable timesteps break the symplecticity of our integrator (see, e.g. [58] and [59], and discussion therein), and the use of softening and tree gravity introduces force calculation errors that can cause drift in the accuracy of our calculations. To estimate the simulation accuracy and to ensure our system maintains time-symmetry, we can consider only the large body subsystem (without any impactor or fragments; i.e. Phase 3 and 4), and compare computed quantities to an appropriate benchmark. The drift in the integrals of the motion (energy, angular momentum, and linear momentum) relative to their initial values are presented in the left panel of Fig. 5. In the right, the semimajor axis, eccentricity, argument of pericenter, and change in the time of pericenter passage of the Earth's orbit are presented relative to values obtained using the JPL HORIZONS system.

To ground the discussion on these drifts, we should estimate the contributions from force softening, which could dominate drift in the integrals of the motion. One way to estimate this is to compute energy drift relative to the true potential energy, not due to the softened

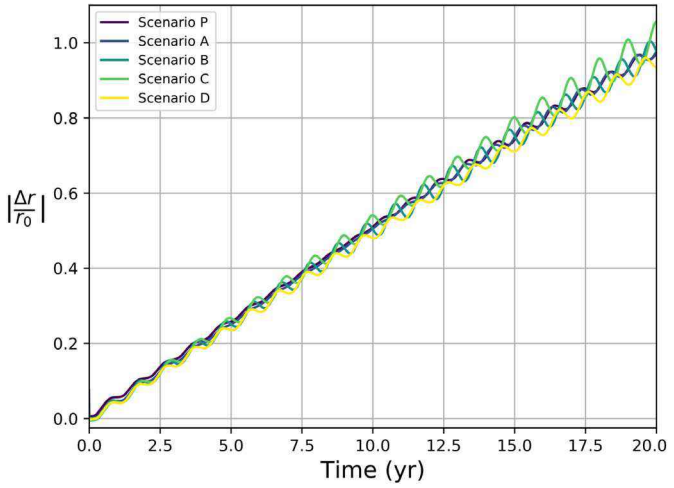

Fig. 6. Relative difference in the position of the Earth as computed in our simulations relative to the reference position in the JPL HORIZONS database, for all five scenarios considered in this study. The normalization by r_0 naturally expresses this distance in AU; neglecting the small perturbations, the linear growth in phase error is clearly visible.

potential. For a virialized system $\left(1 + \frac{T_0}{U_0} = \frac{1}{2}\right)$, the relative drift in the total energy introduced by softening the potential are

$$\left|\frac{\Delta E}{E_0}\right| = \frac{\sum_{i\neq j} U_{0,ij}\left(\sqrt{1+\frac{\varepsilon^2}{r_{ij}^2}} - 1\right)}{U_0\left(1+\frac{T_0}{U_0}\right)} \simeq \frac{\sum_{i\neq j} U_{0,ij}\frac{\varepsilon^2}{r_{ij}^2}}{\sum_{i\neq j} U_{0,ij}}. \tag{30}$$

We bound this ratio, $\frac{\varepsilon}{r_{ij}}$, in Phases 3 and 4 according to the softening length selection scheme outlined in Section 3.3, and therefore our

energy drift is approximately bounded by

$$\left|\frac{\Delta E}{E_0}\right| \lesssim \frac{f_{max}}{1-f_{max}} \simeq f_{max}, \tag{31}$$

where f_{max} is the maximum allowable force error, which (per Section 3.3) is set to 10^{-5}. This is indicated in Fig. 5. This estimate bounds the drift from the force softening alone, but is only a crude estimate to give the order of how large it could grow, and is violated whenever the instantaneous Cartesian state vectors of the system are not virialized[16] or the particle separations are much larger (and therefore the energy calculation much more accurate.) Nevertheless, it is a useful bound to consider.

The relative energy drift presented in Fig. 5 demonstrate that our calculations are satisfactory to at least to the maximum allowable force error chosen in Section 3.3. For each integral of the motion, the drifts accumulate to some roughly asymptotic value by about 2.5 years. However, drift in the integrals of the motion is not the only source of errors in our calculation. Orbital phase errors will accumulate over time and eventually destroy the fidelity of the simulation. To estimate this, the plots of the osculating orbital parameters of the Earth in Fig. 5 are useful. Relative to the errors in the JPL HORIZONS orbital elements, the semimajor axis, eccentricity, and argument of pericenter errors are much larger, but do not appear to display secular growth over the simulation time. In contrast, the time of pericenter passage displays familiar linear growth behavior (see, e.g. [58].) These phase errors can be seen also in Fig. 6, where we present the relative distance of the Earth in our simulations to the position found in the JPL HORIZONS database, measured relative to the initial (small) error at the beginning of the simulation phases 3 and 4. Much like the time of pericenter passage, the relative distance error grows approximately linearly with time. In either case, the secular orbit errors appear to be somewhat tolerable below at least a single impactor period for each scenario. Our simulations also have the advantage that during Phase 4, when the fragment orbits are integrated forward, the system will evolve closer to a state of higher accuracy.

These errors should also be considered in the context of time-reversal symmetry. We have plotted both Phase 3 and 4 in Fig. 5; the time axis corresponds to the time until the system returns to the Earth impact state at $t = 0$ years. Thus the Phase 3 errors start at $t = 0$ and continue forward to $t = 20$ years; Phase 4 proceeds from $t = 20$ years to $t = 0$ years. The two are indistinguishable from each other at the scale of the reported error, which demonstrates an important point: relative to the errors, there is very little difference in time-reversal symmetry. This is despite the formal breaking of this symmetry by adopting variable timesteps and tree gravity. In this regard, we find that our system maintains approximate time-reversal symmetry to a high enough degree that our time-reversal strategy used in Section 3.2 used to produce accurate initial conditions is justified; this is also reflected in that impacts are achieved reliably in our tests of the system.

We should consider the origin of both the drift in the integrals of the motion and the orbital phase errors. For each of the measures presented in Figs. 5 and 6, versions of the simulation were run in which some of the approximations described in previous Sections were discarded in favor of a more expensive scheme. The oct-tree gravity was compared against direct summation to verify that the physics package as implemented in Spheral++ appropriately reduced to direct summation in the absence of closely separated particles. Schemes with no softening were found to have a far greater accuracy in the integrals of the motion (with energy errors on the order of 10^{-10}), but we found no functional difference in the accuracy of the osculating orbital elements of the Earth in Fig. 5 or the relative distance errors as presented in Fig. 6. Similarly, we compared our system using both a variable timestep (using the scheme described by Eq. (8)) and using a range of constant global timesteps of the same order. We find also that the accuracy of the integrals of the motion is marginally improved by constant timesteps, but as the errors are dominated by softening, this difference is only distinguishable when softening is turned off. Further, we find no improvement in the orbital phase errors using constant timesteps. The origin of these errors could be our low-order integrator, and could also be augmented by our neglect of contributions from the many other solar system bodies that we do not include in our simulation, as well as any non-gravitational forces. Ultimately, because we are focusing on short times-to-impact (below one year), we regard these errors as tolerable and should not affect our results more than the other approximations we have adopted. However, improvements such as higher order integrators could improve the fidelity of our simulations, which we will explore in future work.

4. Nuclear disruption assessments for specific scenarios

4.1. Scenario assessment design

For the individual scenario studies, it is desirable to span a wide range of times-to-impact: this will allow us to examine the disruption strategy as a function of this critical limiting parameter. In addition, it is known from studies of deflection [11] that the direction in which a deflection is directed matters to long term success of the mission; deflections oriented along the direction of the orbit of the target lead to secular enhancement of the orbital deflection and therefore is the superior choice for such missions. However, such enhancements are magnified on the timescale of the orbital period of the target. It has been shown that over sub-period timescales, the optimal deflection direction is not necessarily in-orbit [60,61]. Thus, the specific characteristics of the scenario may result in other preferred directions, which should be explored. As we have adopted a two-velocity parameterization (see Section 3.4) we will explore this through the direction of the deflection component of the disruption. We will consider not only the in-orbit, deflection-optimal direction (denoted *Orbit*), but also directed along the radius vector from the solar system origin (denoted *Radial*), and the remaining direction that completes the basis that tends to increase inclination and induce motion orthogonal to the ecliptic (denoted *Ecliptic*). These directions correspond to the basis for the comoving Hill frame[17] of the target (with Cartesian directions y, x, and z respectively.) Lastly, though we have identified our fiducial velocity scaling in Section 2, it is desirable to bracket the scenarios by conducting an evaluation of disruptions at lower efficiency. We will thus conduct series of simulations in which we use the nominal velocity scalings derived from our disruption simulations, and series in which we scale those down by a factor of 10. (This corresponds to a naive energy, and therefore device yield, scaling reduction of a factor of 100.) In terms of disruption robustness, scaling the velocities down by a factor of 10 still results in relative neighbor velocities generally larger than the progenitor escape velocity (see Fig. 3), and the scaled kinetic energy per mass remains much greater than $Q*_D$ estimated for objects of this size.

Specifically, we will use a common structure for each scenario. Each assessment will consist of six series of simulations — two velocity scalings (Nominal and Reduced), and three deflection directions (Orbit, Radial, Ecliptic). Each series will be consist of a series of 128 different times-to-impact between 0.25 and 6 months, spaced logarithmically to sample shorter times more efficiently. The Nominal scaling will use a 46.96 m/s deflection velocity, and disruption velocities sampled from

[16] Since the virial theorem applies to time-averages of the total kinetic and potential energies, it is possible for a virialized system to depart from virial values provided the averages remain virialized.

[17] The Hill frame is a local reference frame with the x-axis directed away from the orbit focus and the z axis directed parallel to the orbital angular momentum vector.

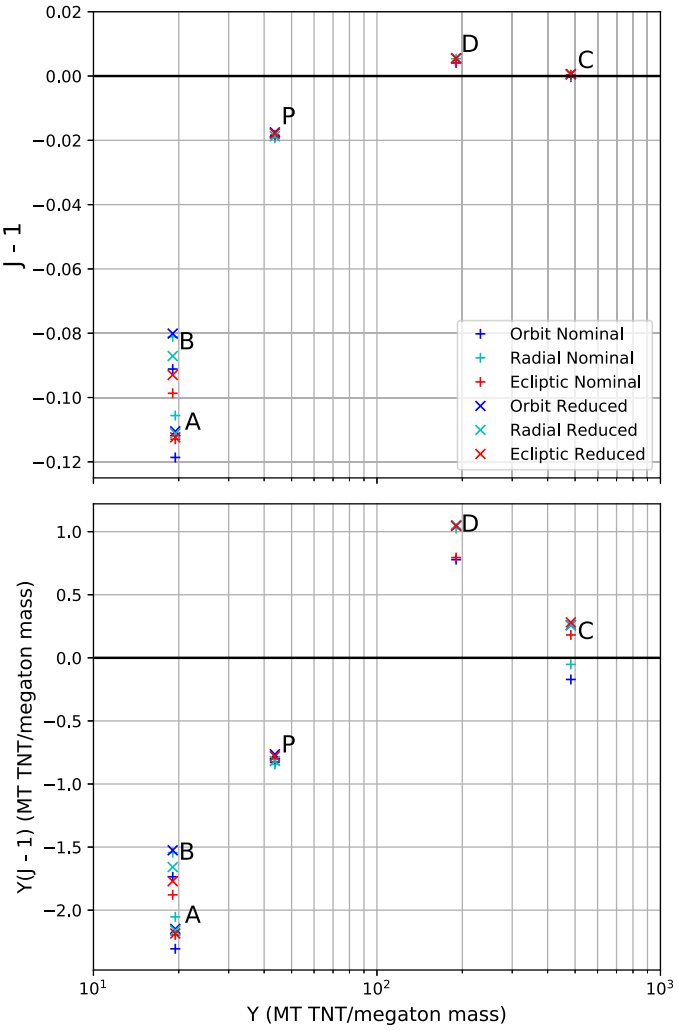

Fig. 7. Fractional reduction (top) and total reduction (bottom) in the nominal impact energy potential for each scenario, constituting the energy reduction that occurs only from changing the fragment velocities (not reducing impacting mass). The color of the symbol indicates the direction of the deflection direction (blue, in-orbit; cyan, radial; red, ecliptic); the shape indicates whether the nominal (pluses) or marginal (crosses) velocity scaling was used. (For interpretation of the references to color in this figure legend, the reader is referred to the web version of this article.)

a lognormal distribution with mean 48.89 m/s and a FWHM of 0.4795 dex, consistent with those obtained in Section 2.2. The deflection and disruption mean velocities are scaled down by 10; the FWHM is unchanged. This structure provides a comprehensive study across all five scenarios that covers the parameter space necessary for a high-fidelity assessment and can be simply compared between scenarios to generalize their results. Lastly, each individual simulation used a total target mass of 10^{12} grams (one megaton mass) partitioned over 2000 individual equally sized fragments (chosen to balance computational expediency with impacting mass accuracy); though smaller than the nominal mass used in Section 2, the total mass used in our N-body simulations is close to the total mass of the bulk particles used to characterize the disruption simulations in Section 2.2 and simplifies scaling arguments.

4.2. Impact fraction and impact energies

The most natural figure of merit in assessing the risk of disruption events – either in terms of the effectiveness of preventing a large impactor from hitting the Earth, or in terms of the costs of such a strategy in terms of risk reduction – is the impact fraction:

$$I = \frac{1}{M_{imp}} \sum_i m_i, \tag{32}$$

where the sum is taken over all i fragments (with masses m_i) whose trajectories result in entry into the Earth's atmosphere. (In our simulations, an impact is registered when the distance between a fragment and the Earth becomes less than an Earth radius. This is tracked by a sentinel that checks at every timestep whether this occurs for any fragment. If an impact occurs, the fragment's properties are recorded and the fragment is removed from the calculation.) The consequences of fragmentation scenarios are sometimes quoted instead as an impact likelihood, as in [17], or impact probability in [18], but the impact fraction implies a more natural definition in terms of the efficiency of eliminating impacting mass. This is necessarily a simplistic assessment of risk, as it weighs equally scenarios in which the total impacting mass is the same, even though a single monolithic mass and many smaller and well dispersed fragments with the same total mass might have dramatically different consequences. We will not consider atmospheric entry in this work for risk assessment, and so our results should be interpreted as risk upper bounds; such efforts have been successfully integrated in systems based on the Clohessy–Wiltshire–Hill equations in [19] and [9]. Nevertheless, it provides a means to quantify worst case risks for particular mission choices, as the risk should be approximately maximized under the assumption of a monolithic fragment with a mass equal to $I M_{imp}$ for a given mission with impact fraction I.[18] Overall, our approach affords the impact fraction a natural interpretation relative to this worst-case scenario: since impact effects scale with the energy of the impactor, these effects should scale nearly linearly with the impacting mass [62,63].

Though the impact fraction should provide a good estimate of threat reduction, a true estimate should evaluate the distribution of impacts on the Earth and provide an impact energy for each one. Within the Earth-Centered Inertial (ECI) coordinate system, the relative velocity of a fragment i at impact should be (including the Earth's coordinate rotation) [19]:

$$\mathbf{v}_{i,ECI} = \mathbf{v}_{i,SSB} - \mathbf{v}_{\oplus,SSB} - \frac{1}{r^2_{\oplus,SSB}} \left(\mathbf{r}_{\oplus,SSB} \times \mathbf{v}_{\oplus,SSB} \times \mathbf{r}_{i,rel} \right). \tag{33}$$

where $\mathbf{r}_{i,rel} = \mathbf{r}_{i,SSB} - \mathbf{r}_{,SSB}$ is the relative position of the fragment in the Solar System Barycentric (SSB) frame, and the quantities labeled with SSB indicate Solar System Barycentric quantities. In practice, the correction from the coordinate rotation is typically small, being of order

Table 3
Some useful properties of the hypothetical impactor for each Scenario described in Section 3.5: the relative velocity at impact in the SSB frame, neglecting the effects of the Earth's gravity; the expected enhancement to the Earth's effective radius due to gravitational focusing; the relative velocity of the impactor in the ECI frame; and the normalized impact energy per impactor mass, Y/M, in units of megatons of TNT equivalent energy per megaton mass.

Scenario	$v_{rel,SSB}$ (km/s)	$\sqrt{\sigma/\sigma_{geo}}$	$v_{rel,ECI}$ (km/s)	Y/M (MT TNT/ megaton mass)
P	15.49	1.223	19.11	43.66
A	5.919	2.137	12.76	19.44
B	5.787	2.175	12.62	19.04
C	62.59	1.016	63.58	483.1
D	38.29	1.042	39.90	190.2

[18] We also note that, since we are not considering true fragmentation in this work, we do not include the effects that a fragment distribution would have on the impact fraction. Future studies should include this as part of the risk assessment.

$\frac{r_{i,rel}}{r_{\oplus,SSB}}$. For comparison between scenarios, Table 3 provides the relative velocity in the SSB frame without mutual gravitational effects and the final velocity within the ECI frame including these effects, as well as the expected enhancement of the Earth's cross section due to gravitational focusing (see Section 3.3.) This reference impact energy can be used to compare against the total impact energy in each disruption scenario to evaluate the impact fraction as a metric of disruption effectiveness. The total impacting energy is

$$E = \sum_i \frac{1}{2} m_i v_{i,ECI}^2 \tag{34}$$

We compare this to the nominal impact energy associated with the scenario, $Y = \frac{1}{2} M_{imp} v_{imp,ECI}^2$. Since the velocity changes due to disruption are relatively small compared to the relative velocity to the Earth, we expect

$$E \propto IY. \tag{35}$$

We found that this proportionality does approximately hold: after correcting for the impact fraction dependence, the difference between E and IY corresponded to a proportionality constant near unity. This corresponds to a change in the total impact energy potential of the system by a few percent. Quantitatively, we can express this reduction in a quantity similar to the impact fraction:

$$J = \frac{E}{IY} = \frac{\sum_i m_i \left(\frac{v_{i,ECI}}{v_{imp,ECI}} \right)^2}{\sum_i m_i} \tag{36}$$

J has a natural interpretation when the fragments are all the same mass, as then it becomes simply the average squared fragment impact velocity relative to the original target's impact velocity. (Varying fragment size is therefore a mass-weighted average.) J was different for each scenario, but had little scatter within the same scenario with different deflection directions and disruption scaling, which is consistent with the disruption event reducing the impact energy potential at the time of the disruption and not over a longer period; the values are easier to visualize as in Fig. 7, where $J - 1$ is plotted against the scenario Y/M for all 30 series of simulations. ($J - 1$ is plotted to emphasize the reduction, or increase, of impacting energy relative to nominal.) The largest reductions appear to be in the Earth-like orbits (A and B), and in some cases of Scenarios C and D, the impact energy can be increased by a very small amount. To visualize the total energy reduction, we plot $Y(J-1) = \frac{E}{I} - Y$ also in Fig. 7. the total energy change is only at most few MT TNT/megaton mass. More systematic studies should be done to establish whether this effect (as large as ~10% in the Earth-like orbits) could be used to optimize disruption scenarios.

4.3. Case study P: PDC 2019

The impact fractions I and impact energies E thus obtained for these six series of simulations for Scenario P are plotted in logarithmic scale in Fig. 8. Broadly, the simulations using the nominal velocities can achieve a two order of magnitude reduction in impacting mass ($I = 10^{-2}$) in as little as two weeks (0.5 months). At longer times-to-impact, the nominal case is sufficiently effective that the number of fragments used in our simulations are not sufficient to resolve the curve above Monte Carlo noise. The reduced velocity disruption (dashed lines), where the velocities are reduced by a factor of 10, is of course less successful: it can achieve a single order of magnitude reduction in impacting mass by about six weeks (1.5 months). These general trends in outcome for these late-time interventions demonstrates a basic feature of the disruption strategy: the outcome is quite sensitive to the robustness of the disruption, and in turn, to the delivered yield. Nevertheless, the nominal impact fraction reduction, $I = 10^{-2}$ at two weeks for a 1 MT TNT device and a 100-meter impactor, is a substantial improvement over no intervention. The differences between the different Hill frame directions for the deflection are most apparent

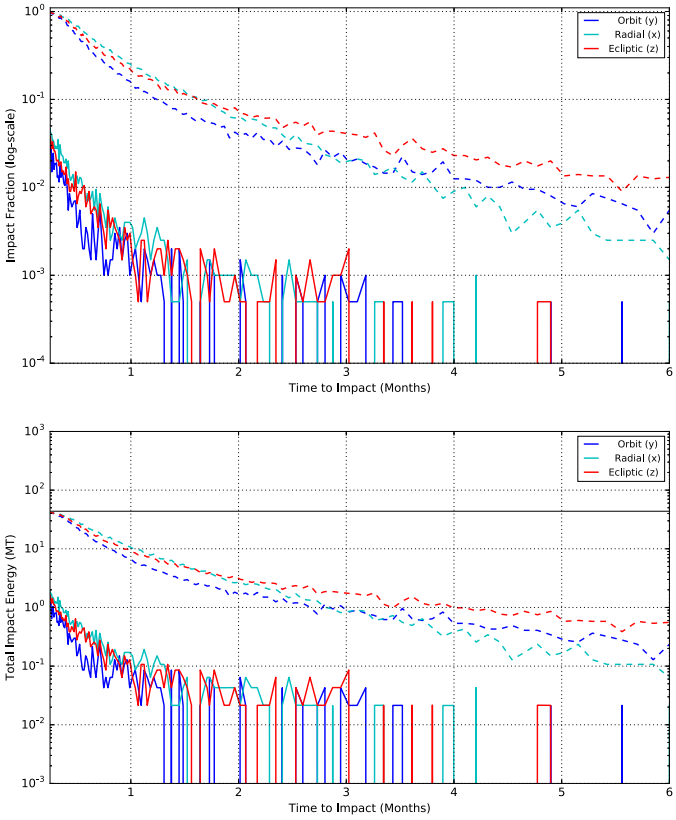

Fig. 8. Impact fractions computed for 128 times-to-impact spanning 0.25 to 6 months for Scenario P. The solid lines indicate those obtained using values for the disruption and deflection velocities from the fiducial disruption simulations (see Section 2). The dashed lines indicate those same velocities scaled down by 10. The blue lines indicate simulations carried out in which the direction of the deflection velocity was oriented in the direction of the orbit; cyan, in the radial direction; and red, out-of-plane. (For interpretation of the references to color in this figure legend, the reader is referred to the web version of this article.)

in the reduced velocity case. For most of the times-to-impact, the out-of-plane deflection (red) performs the worst, falling off less rapidly than the other directions. The radial direction (cyan) is initially more like the out-of-plane deflection, but falls off below that case at around 2.5 months. In this scenario, the in-orbit deflection (blue) tends to outperform the others in both the nominal and reduced velocity cases, which coincides with the typical expectation that in-orbit deflections should perform the best over long time periods [11]. However, even in this case, the differences between the different deflection directions appears to be relatively small. The impact energies bear out the same trends as identified in impact fraction, as expected given that the value of $J - 1$ computed in Section 4.2 was only about 2%.

4.4. Case study 2: 99942 Apophis

The impact fractions and impact energies for the full assessment of Scenario A are plotted in Fig. 9. For the nominal disruption it requires about 1 month to achieve two orders of magnitude reduction in impacting mass; in the more marginal disruption, the impact fraction remains 1 (all fragments impact) for about two weeks before beginning to taper off, indicating that in this Scenario there is a minimum time-to-impact required before disruption begins eliminating impacting mass. In terms of deflection direction, we see different behavior for the two velocity scalings. On the one hand, in the nominal case the radial direction appears to underperform the in-orbit and ecliptic directions until about 1 month. On the other, in the reduced case, there appears to be a moderate reduction of efficiency for the in-orbit direction

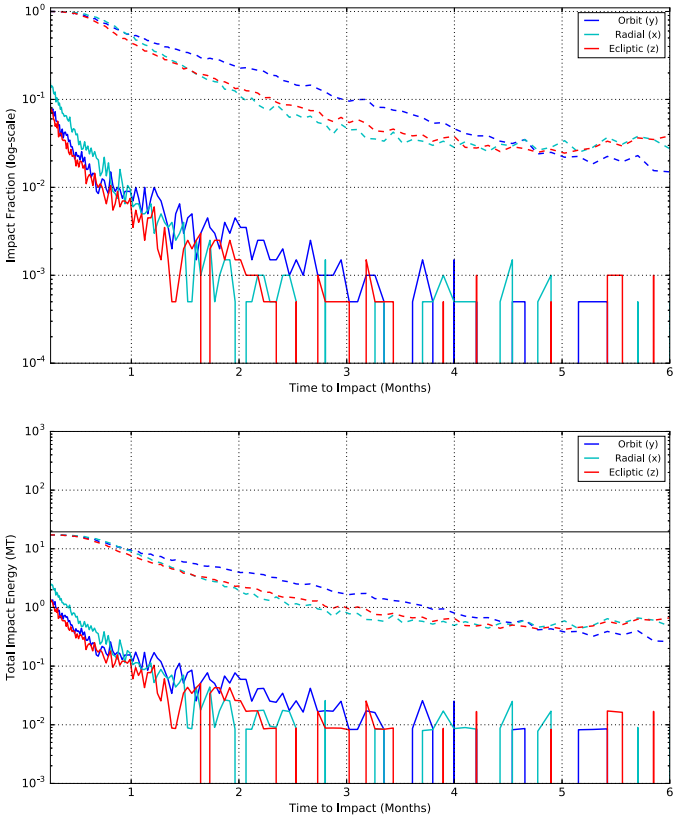

Fig. 9. Same as Fig. 8, but for Scenario A.

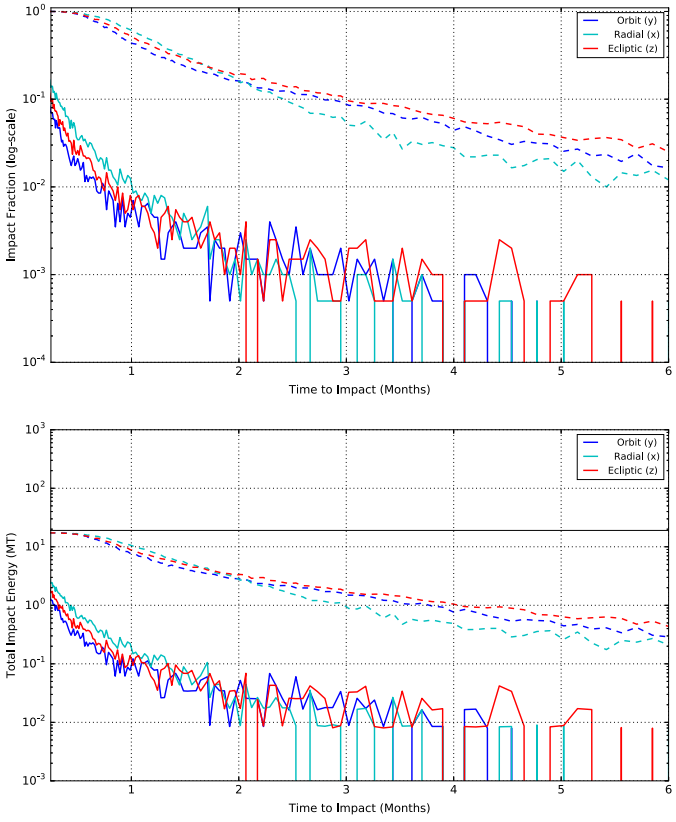

Fig. 10. Same as Fig. 8, but for Scenario B.

relative to the other two choices; relative to the radial and out-of-plane directions at 3 months, the in-orbit direction is ∼20% less effective. However, this advantage becomes weaker with longer time-to-impact, and is lost entirely by essentially 5 months. Remarkably, at this time the impact fraction for the radial and ecliptic directions appears to increase, which is contrary to the expectation that longer times allow larger accumulated deflections and therefore more effective impact fraction reduction. Generally, these counterintuitive behaviors indicate that the particulars of the approach orbit do significantly affect the relative merits of deflection direction, and that choice is not known without dedicating specific scenario studies to evaluate the relative effectiveness of deflection directions. Importantly, the reduced velocity scenarios serve as an important counterexample in demonstrating that the in-orbit direction is not always the best choice, and that the assumptions underlying that recommendation rely on the conditions expected for longer term deflections. These results echo the previously published results concerning optimal deflection direction [60,61], and demonstrate concordance between our approach used in this work and the existing literature.

The impact energy potential reduction for this case was roughly 11%, which is significantly larger than in Scenario P and amounts to a quantitative reduction of impact energy potential of about 2 MT TNT/megaton mass. This can be seen visibly in the impact energies plot, relative to the impact fraction: though the impact energy at 1 month for the nominal velocity case is reduced by more than two orders of magnitude, the impact fraction is nearly exactly two orders reduced. Though of the same order as the changes in JY for the other scenarios, this reduction is significant relative to the total impact potential of this case (see Fig. 7). This reduction, alongside the already much lower impact energy potential (about half relative to Scenario P) balances out the slower falloff in impact fraction for this Scenario. The slower falloff can be simply accounted for in terms of gravitational focusing: because the Earth-like orbits spend a significantly longer time experiencing higher forces from the Earth, it is correspondingly more difficult to move fragments off impact trajectories, as the effective cross section of the Earth is higher and therefore require larger absolute deflections to avoid impact. This is reflected in the large expected gravitational focusing enhancement to the Earth's radius for this scenario in Table 3.

4.5. Case study 3: 101955 Bennu

For Scenario B, the full assessment impact fractions are presented in Fig. 10. The resulting impact fractions are broadly similar to Scenario A, indicating commonality between different scenarios with similar orbital parameters. In the nominal velocity case, we find similarity also in the deflection direction: the radial direction tends to underperform relative to the other two directions, at least at early times (when our simulations can resolve the differences) but this difference is relatively modest. However, in the reduced velocity case, we do not see distinct advantages in any of the deflection directions until roughly 2.5 months, at which time the radial direction becomes apparently superior, contrary to the nominal velocity case. Further, there is no sign of any apparent increase in impact fraction seen at later times, as seen in Scenario A. Also in common with Scenario A, the reduction in impact energy potential ($J-1$) is significant, relatively speaking, though slightly more modest (closer to ∼ 9%.)

4.6. Case study C: (343158) 2009 HC82

The full assessment impact fractions for Scenario C are presented in Fig. 11. Relative to Scenarios P, A, and B, Scenario C is somewhat exceptional, having a retrograde orbit. Because of this it has a very high relative velocity to the Earth and correspondingly a very low gravitational focusing enhancement (see Table 3). The impact fraction shares many characteristics with Scenario P, but falls off marginally

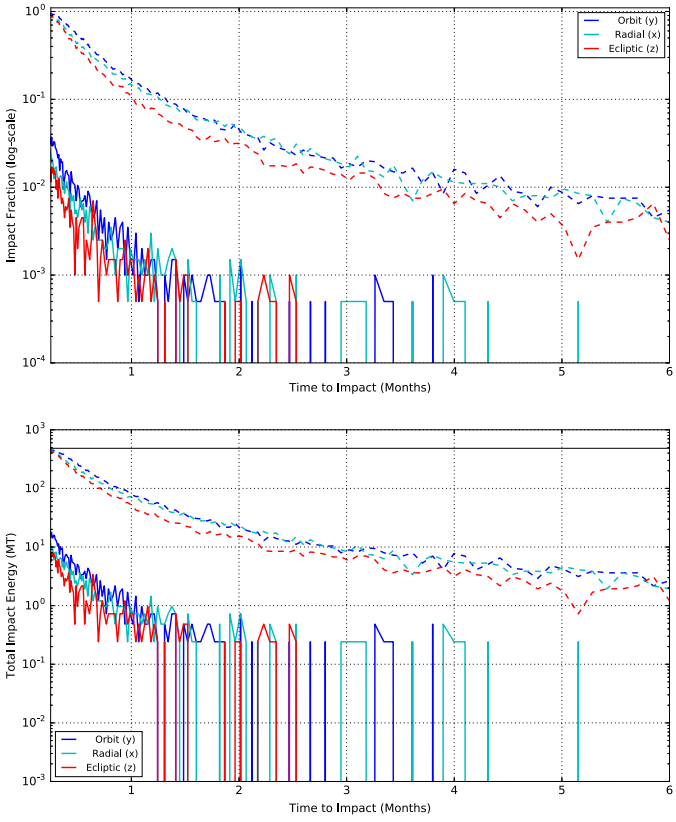

Fig. 11. Same as Fig. 8, but for Scenario C.

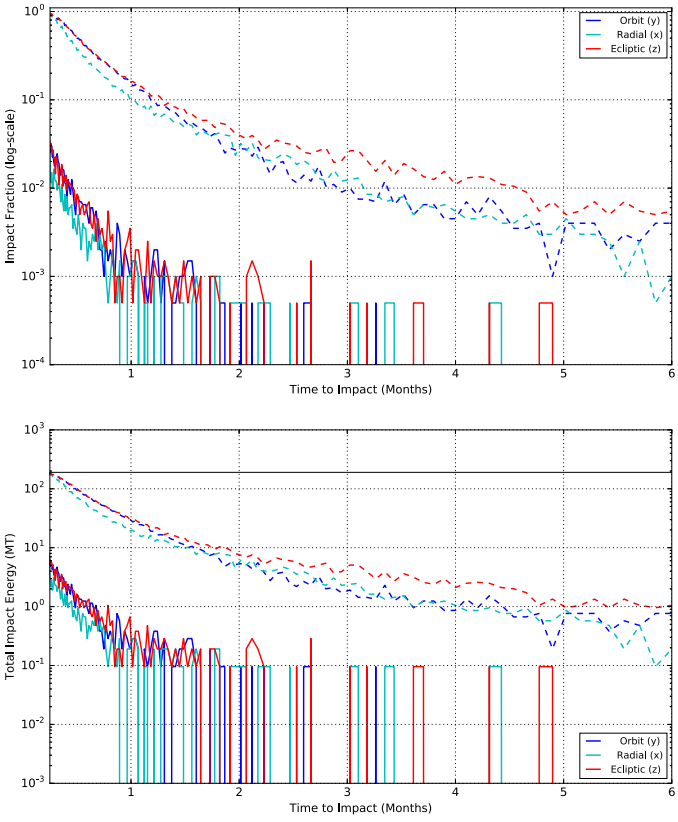

Fig. 12. Same as Fig. 8, but for Scenario D.

faster; an impact fraction of $I = 10^{-2}$ is achieved quite rapidly in the nominal velocity case, by roughly 1 week even for the poorest performing deflection direction (the in-orbit direction.) Put another way, by 1 month the nominal velocity case is capable of reducing the impact fraction to a part in a thousand. Similarly, in the reduced velocity case an impact fraction of $I = 10^{-1}$ is achieved by roughly 1 month. However, the superiority of the impact fraction reduction in this case must be balanced by comparing the total impact energy: though relatively speaking the scenario is much improved, the impacting energy at 1 month is still about an order of magnitude larger than the comparable energies in Scenario A. Continuing a theme observed in the previous three scenarios, the preferred deflection direction appears to depend on the particulars of the orbit — in this case, both the in-orbit and radial directions modestly underperform the ecliptic direction, in both the nominal and reduced velocity cases.

4.7. Case study D: (5496) 1973 NA

Lastly, the full assessment impact fractions for Scenario D are presented in Fig. 12. Scenario D also presents an exceptional case, being highly inclined (68°) and, unlike the other four scenarios, impacting on the dayside of the Earth. It also has a relatively high relative velocity, though not as high as Scenario C. Broadly speaking the impact fractions (Fig. 12) are very similar to those of Scenario C, underperforming slightly in terms of that metric. However, the impacting energies are naturally somewhat lower. Also in common with Scenario C, there are two deflection directions which underperform the other, but in this scenario, it is the radial direction that is superior. In the reduced velocity case, the in-orbit direction is nearly identical to the ecliptic direction until about 1.5 months to impact, after which it falls relative to that direction and follows instead the radial case. Scenario D is also unusual as noted in Section 4.2, in that the velocity adjustment leads to a modest increase in impacting energy potential, but this is relatively small (on the order of less than half a percent), and is overwhelmed entirely by the sheer reduction in impacting energy potential relative to the extremely high impact velocities of Scenario C.

4.8. Discussion

Overall we can establish a few trends using these five case studies as an ensemble. The first basic trend is that there is a tradeoff between nominal impact energy and how quickly disruption strategies become effective. Cases C and D have very little gravitational focusing enhancement and spend comparatively little time subject to strong gravitational influence from the Earth, and so the minimum delta-v threshold necessary to begin reducing impacting mass is much lower. On the other hand, the impact energies are much higher, and as a result, each impacting fragment maintains much more energy and therefore a smaller impact fraction is necessary to achieve the same reduction in total impact energy. For Scenarios A and B, the opposite is the case: their impact energies are already quite low in relative terms, but because they are much more strongly affected by gravitational focusing, it is necessary to disrupt them either more robustly or earlier in time. This tradeoff should factor into policymaker's decisions: at the very least, it is not just physical size but also the specifics of the impactor's orbit that can affect the effectiveness of a disruption mission. Regardless of the scenario chosen, however, a reduction of impact fraction (and hence, roughly, impact energy) by two orders of magnitude is achievable for a 100-meter diameter object given a month in advance of impact, and depending on the particulars of the orbit, can achieve three orders of magnitude in the same timeframe. Incorporating gravitational focusing was a key part of this assessment, and therefore it is crucial that gravitational focusing be included in future assessments of disruption risks and effectiveness.

Additionally, some interesting properties in the disruption scenarios emerged that could affect mission planning in a direct way. The first of these was discussed in Section 4.2, in which the disruption altered the velocities of the fragments such that, controlling for the impact fraction, the total impact energy potential was changed, in some cases (Cases A and B) reducing the impacting energy by about 10%. This is a significant reduction and could be worth exploiting in a disruption scenario. The second was that the direction of the deflection appeared to be less of a deciding factor than in pure deflection scenarios. This may be surprising in the context of these deflection studies with long times-to-impact, in which deflections are typically chosen in the direction of the orbit to maximize the secular increase in orbit deflection [11]; however, as reported previously in [60,61], the optimal deflection direction may not coincide with the in-orbit direction over short periods. These results suggest that, at least for these late-time, short times-to-impact, driving the body strongly enough to overcome gravitational focusing is a more important consideration than precise prediction of deflection direction. Were this not the case, success could be contingent on the specific deflection direction, which adds additional uncertainty to mission planning and is likely dependent on the interior of the impactor. This might not be as great of a concern, which in turn may enable mission planning to operate with fewer restrictions on targeting a standoff burst. However, in some cases there can be a moderate improvement in outcome for certain deflection directions, and this direction may be scenario-dependent, so care must be taken to study any potential real scenario in great detail for mission planning. In particular, using tools such as those presented in this work or Keplerian-style approaches, it is possible to identify the optimal deflection direction for disruption scenarios in advance.

Lastly, some surprising features which can negatively influence the outcome of disruption strategies emerged that merit further study. The first is that the typical change in impact energy potential, studied in Section 4.2, can in one particular case (Scenario D) manifest as an increase, not decrease. This may not necessarily be unusual: since this adjustment in impacting energy is due to the changes in the relative velocity to Earth of the impacting fragments, then $J - 1 > 0$ would be the result of an increase in their relative velocity to Earth in comparison to the original orbit. This effect should be investigated to ensure that an otherwise apparently successful mitigation does not accidentally worsen the outcome. Additionally, in a few cases (the reduced velocity cases for Scenario A), the impact fraction/impact energy curves were not monotonic with time-to-impact: at roughly 5 months, these cases displayed an apparent increase in these metrics at later times-to-impact. It is possible that this type of behavior occurs due to a particular orientation of the approach orbit to the Earth's; this effect merits further exploration to ensure that such effects are predicted and therefore avoided in the planning phase.

We conclude by reiterating the limitations discussed in the above sections regarding our simulation strategy. First, our nuclear disruption simulations are limited in that many details about typical small bodies are not known and consequently the modeling choices for the material response, including our neglect of fragmentation, introduces uncertainty in our predictions for the disruption of the body. As the state-of-the-art in nuclear disruption modeling advances, our approach outlined here can nevertheless incorporate those results in a straightforward manner. Second, despite our aim to advance the sophistication of the gravitational physics governing the orbits of the fragments using N-body methods, our approach still suffers from several limitations as outlined above. Strict time-reversal asymmetry, integration errors, and aggressive softening relative to the fragment–fragment separation may introduce uncertainty in our results. For that reason, the results presented in this work should be understood as estimates that will improve as better algorithms and methods are implemented.

5. Conclusions

To summarize:

1. We present a fiducial ASPH disruption simulation carried out with Spheral++ (Section 2) and use it to establish a basic model for the initial conditions for the new fragment orbits that would be used to determine their new orbits. We find that for a 100-meter scaled model of 101955 Bennu (with mass equal to about 10^{12} grams) that a 1 MT TNT equivalent device at a standoff height of 15 meters above the equator (65 meters from the center) is sufficient to robustly disrupt it, producing a fragment field whose center-of-mass velocity (corresponding to an equivalent deflection) is 46.96 m/s. Within the center-of-mass frame, the disruption was found to be nearly spherically symmetric and radial, with a rough distribution of velocity magnitudes centered at 48.89 m/s.
2. In Section 3, we describe the gravitational simulation scheme used to compute the new fragment orbits following a disruption event, carried out using the N-body methods of Spheral++ (but are generally applicable to any N-body code.) We describe the routines used to select a hazardous orbit in Section 3.2; the effects and treatment of the initial orbit kick and gravitational focusing by the Earth in Section 3.3; how the fragments are initialized and their self-gravity treated in Section 3.4; what specific scenarios we study in Section 3.5; and the drift in our simulations in Section 3.6. We discuss the general structure of our scenario assessments in Section 4.1.
3. Next, in Section 4.2, we discuss the impact fraction as a basic figure of merit, and compare it with the total impacting energy. We find that when we compare the energy of the intact impactor that the disruption can reduce the total amount of impacting energy by altering the velocities of the fragments and hence placing them on different impacting trajectories. In the case of Earth-like orbit scenarios (A and B), this reduction can be significant (of order 10%). In other cases, impact energy can even be enhanced by a small amount (Scenario D, 0.3%).
4. Then in Sections 4.3 to 4.7, we present detailed estimates of each scenario described in Section 3.5 using the fiducial velocity distribution values from Section 2, including both the nominal velocities and velocities scaled down by a factor of 10. For each of these cases, the nominal disruption was sufficient to reduce impacting mass by two orders of magnitude by at most 1 month of time-to-impact. In Section 4.8 we provide some general observations obtained from our studies. The first point is an apparent tradeoff between impact energy and rate of disruption hazard reduction: where more Earth-like orbits tend to have lower impact energies, they spend more time subject to gravitational focusing and thus require higher disruption velocities or longer times-to-impact to achieve the same risk reduction as less Earth-like orbit. Conversely, the more eccentric or retrograde orbits tend to have much higher impact energies, but because they are subject to less gravitational influence from the Earth, disruption is more effective at later times-to-impact than more Earth-like orbits. Additionally, we find that the direction of the deflection is less important for robust disruptions, though there is some modest variation that could be exploited by a prepared planner. Lastly, there are a few potential hazards to disruption performance that should be studied in more detail in order to avoid them in real scenarios.

Declaration of competing interest

The authors declare that they have no known competing financial interests or personal relationships that could have appeared to influence the work reported in this paper.

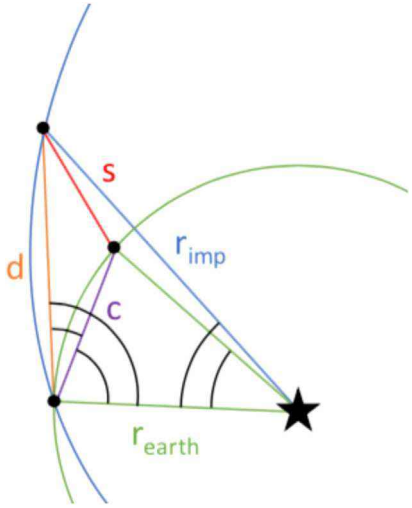

Fig. A.13. Geometry of the Earth-impactor distance problem. The distance s is computed to third order accuracy in δE in Appendix.

Acknowledgments

The authors would like to thank the anonymous referees for their extensive comments and suggestions which improved the quality of the manuscript. PKK was supported by a Livermore Graduate Scholarship at Lawrence Livermore National Laboratory, and acknowledges the Jefferson Scholars Foundation for additional support through a graduate fellowship. This work was also provided additional support through JHU/APL internal funding. The authors acknowledge the MATPLOTLIB library [64], which was used in producing most of the plots in this work, with the exception of Fig. 1, which made use of the visualization tool VISIT [65] and the object file viewing capabilities of XCODE. This work was performed under the auspices of the Department of Energy by Lawrence Livermore National Laboratory under Contract DE-AC52-07NA27344. LLNL-JRNL-778288.

Appendix. Third order earth-impactor distance and orbit timing

In Section 3.3 the need to determine the absolute distance between the Earth and the impactor for short times prior to impact was asserted. This problem amounts to a calculation of the distance between two points on different orbits at some relative time, δt. We will assume in this treatment that the Earth's orbit is circular and work in AU units for distance. For simplicity, we treat this problem as if the two orbits are coplanar. Any mutual inclination of the orbits will make the actual Earth-impactor distance at some δt to impact larger than that calculated here, as an Earth impact necessarily occurs at a node. As a result, the computed δt provided here should result in a Earth-impactor distance greater than the constraint distance. The geometry of the problem is indicated in Fig. A.13.

We will solve for the short change in eccentric anomaly, δE, between the final impactor position at E_0 (which coincides with the Earth) and the eccentric anomaly at a position that is at least some distance, r_{tol}, away from the Earth:

$$E = E_0 - \delta E. \tag{A.1}$$

The final eccentric anomaly, E_0, is given by orbital parameters:

$$E_0 = \arccos\left(\frac{1}{e_{imp}}\left(1 - \frac{1}{a_{imp}}\right)\right). \tag{A.2}$$

The law of cosines provides an expression for the Earth-impactor distance:

$$s^2 = d^2 + c^2 - 2dc\cos\beta. \tag{A.3}$$

First, we consider the elliptic chord distance d which is also provided by the law of cosines and the eccentric anomaly difference:

$$d^2 = 1 + r_{imp}^2 - 2r_{imp}\cos\delta E, \tag{A.4}$$

where r_{imp} is given by

$$r_{imp} = a_{imp}\left(1 - e_{imp}\cos E\right). \tag{A.5}$$

Next we consider the circular chord c, which is part of an Isosceles triangle where the apex angle is determined by orbit timing:

$$c = 2\sin\left(\frac{n_\oplus \Delta t}{2}\right), \tag{A.6}$$

where $n_\oplus$ is the Earth's mean motion and Δt is the timing corresponding to the traversal between E and E_0. This must be found using the Kepler equation, noting that the impactor's mean motion is simply related to the Earth's mean motion by $n_{imp} = n_\oplus a_{imp}^{-3/2}$:

$$\Delta t = \frac{a_{imp}^{3/2}}{n_\oplus}\left(\delta E - e_{imp}\left(\sin E_0 - \sin E\right)\right). \tag{A.7}$$

(This will be used once δE is determined to determine the desired integration time.) Finally, we need to determine the cosine of the angle β between the elliptic and circular chords. This can be found by computing the difference between the angle θ (in the triangle formed from the final impactor position, the initial impactor position, and the sun) and the angle γ in the isosceles triangle used to determine c. First, θ:

$$\theta = \arccos\left(\frac{1 + d^2 - r_{imp}^2}{2d}\right). \tag{A.8}$$

Next, γ:

$$\gamma = \frac{\pi}{2} - \frac{n_\oplus \Delta t}{2}. \tag{A.9}$$

Using this, $\cos\beta$ can be determined:

$$\cos\beta = \sin\theta\cos\left(\frac{n_\oplus \Delta t}{2}\right) + \cos\theta\sin\left(\frac{n_\oplus \Delta t}{2}\right). \tag{A.10}$$

With this it is possible to compute an expression for s, the Earth-impactor distance, and then employ a rootfinding routine to find the corresponding δE, and thus Δt, for a particular r_{tol}. However, directly employing rootfinding is both slow and often fails to find a correct root. Instead, we employ MATHEMATICA [66] to compute a series expansion in δE, noting that the distances we desire likely correspond to small eccentric anomaly differences. The resulting approximation to third order is:

$$\begin{aligned} s \simeq\ & \left(3a_{imp} + a_{imp}^2\left(e_{imp}^2 - 1\right) - 2\sqrt{a_{imp}}\right)^{1/2}\delta E + \\ & \frac{3\left(a_{imp} - \sqrt{a_{imp}}\right)\left(a_{imp}^2\left(e_{imp}^2 - 1\right) + 2a_{imp} - 1\right)^{1/2}}{2\left(3a_{imp} + a_{imp}^2\left(e_{imp}^2 - 1\right) - 2\sqrt{a_{imp}}\right)^{1/2}}\delta E^2 + \\ & \left(\left(15a_{imp}^4 - 12a_{imp}^{7/2}\right)\left(e_{imp}^4 - 2e_{imp}^2 + 1\right) + \right. \\ & - 4a_{imp}^3\left(e_{imp}^4 - 17e_{imp}^2 + 16\right) - 48a_{imp}^{5/2}\left(e_{imp}^2 - 1\right) + \\ & - 18a_{imp}^2\left(3e_{imp}^2 - 7\right) + 4a_{imp}^{3/2}\left(10e_{imp}^2 - 31\right) + \\ & \left. -72a_{imp} + 120\sqrt{a_{imp}} - 37\right) \times \\ & \left(24\left(a_{imp}^{3/2}\left(e_{imp}^2 - 1\right) + 3\sqrt{a_{imp}}\right)\right)^{-1}\delta E^3 + \mathcal{O}\left(\delta E^4\right). \end{aligned} \tag{A.11}$$

MATHEMATICA can conveniently produce a form close to PYTHON code using the `FortranForm` function. Comparisons of the first, second, and third order approximations for the Earth-impactor distance for δE up to $\pi/4$, and their relative errors, are provided in Fig. A.14 for each scenario considered in this work (see Table 2). The errors in the third order approximant are well-bounded even for eccentric anomaly distances of up to $\pi/8$, a relatively large fraction of the impactor's orbit.

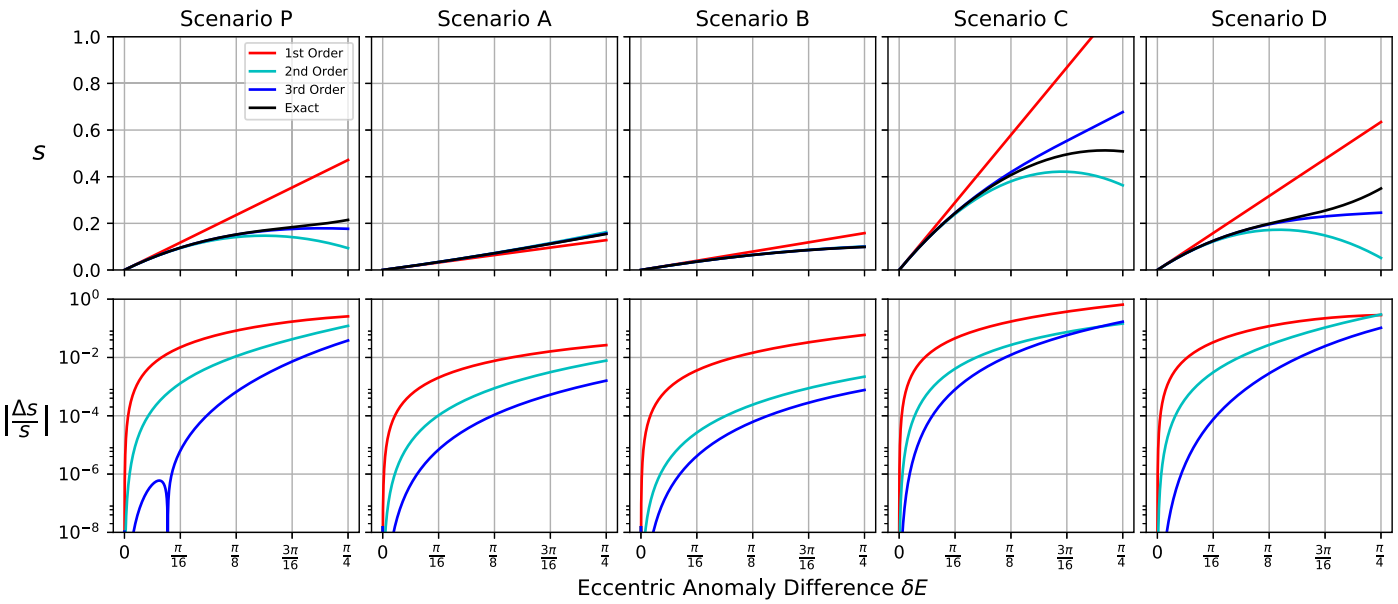

Fig. A.14. Comparison of the exact (black) Earth-impactor distance to the first (red), second (cyan), and third (blue) order approximations determined in Appendix (top row) and the corresponding relative errors (bottom row) as functions of the relative change in eccentric anomaly δE for the five scenarios described in Section 3.5 (columns). For all scenarios, the relative error in the third order approximant is bound at or below a part in a hundred for all scenarios provided $\delta E \leq \pi/8$. (For interpretation of the references to color in this figure legend, the reader is referred to the web version of this article.)

With this approximation in hand, one can simply compute a solution to the problem by finding the roots of the cubic formed with the terms in Eq. (A.11) and augmenting with a constant term equal to $-r_{tol}$. The positive real root is always chosen. Then, the corresponding integration time can be found using the computed δE, the final eccentric anomaly E_0 (Eq. (A.2)), and Eq. (A.7). This procedure is implemented to bound the force calculation errors for gravitational focusing and avoiding orbital parameter kick from initial close encounters as described in Section 3.3.

References

[1] P. Brown, R.E. Spalding, D.O. ReVelle, E. Tagliaferri, S.P. Worden, The flux of small near-Earth objects colliding with the Earth, Nature 420 (2002) 294–296, http://dx.doi.org/10.1038/nature01238.

[2] L.W. Alvarez, W. Alvarez, F. Asaro, H.V. Michel, Extraterrestrial cause for the Cretaceous-Tertiary extinction, Science 208 (4448) (1980) 1095–1108.

[3] B. Napier, D. Asher, The Tunguska impact event and beyond, Astron. Geophys. 50 (1) (2009) 1–18.

[4] P.G. Brown, J.D. Assink, L. Astiz, R. Blaauw, M.B. Bosloughh, J. Borovička, N. Brachet, D. Brown, M. Campbell-Brown, L. Ceranna, et al., A 500-kiloton airburst over Chelyabinsk and an enhanced hazard from small impactors, Nature 503 (7475) (2013) 238.

[5] National Research Council (Ed.), Defending Planet Earth: Near-Earth-Object Surveys and Hazard Mitigation Strategies, National Academies Press, 2010, URL: https://books.google.com/books?id=PzhkAgAAQBAJ.

[6] C.M. Roithmayr, L. Kay-Bunnell, D.D. Mazanek, R.R. Kumar, H. Seywald, M.A. Hausman, Accurate Determination of Comet and Asteroid Orbits Leading to Collision With Earth, Technical Report, NASA Langley Research Center; Hampton, VA, United States, 2005, URL: https://ntrs.nasa.gov/search.jsp?R=20050186570.

[7] D. Dearborn, 21st century steam for asteroid mitigation, in: 2004 Planetary Defense Conference: Protecting Earth from Asteroids, American Institute of Aeronautics and Astronautics, Orange County, California, United States, 2004, URL: https://arc.aiaa.org/doi/pdf/10.2514/6.2004-1427, AIAA-2004-1427.

[8] M.B. Syal, D.S.P. Dearborn, P.H. Schultz, Limits on the use of nuclear explosives for asteroid deflection, Acta Astronaut. 90 (2013) 103–111, http://dx.doi.org/10.1016/j.actaastro.2012.10.025.

[9] B. Wie, D. Dearborn, Earth-impact modeling and analysis of a near-Earth object fragmented and dispersed by nuclear subsurface explosions, J. Astronaut. Sci. 59 (2014) http://dx.doi.org/10.1007/s40295-013-0008-3.

[10] J.M. Owen, P. Miller, J. Rovny, J. Wasem, K. Howley, E.B. Herbold, Asteroid diversion considerations and comparisons of diversion techniques, Procedia Eng. 103 (2015) 466–474, http://dx.doi.org/10.1016/j.proeng.2015.04.061, URL: http://www.sciencedirect.com/science/article/pii/S1877705815007353, Proceedings of the 2015 Hypervelocity Impact Symposium (HVIS 2015).

[11] D.P.S. Dearborn, P.L. Miller, Defending against asteroids and comets, in: Handbook of Cosmic Hazards and Planetary Defense, Springer International Publishing, Cham, 2015, http://dx.doi.org/10.1007/978-3-319-03952-7_59.

[12] D.S. Dearborn, M. Bruck Syal, B.W. Barbee, G. Gisler, K. Greenaugh, K.M. Howley, R. Leung, J. Lyzhoft, P.L. Miller, J.A. Nuth, C.S. Plesko, B.D. Seery, J.V. Wasem, R.P. Weaver, M. Zebenay, Options and uncertainties in planetary defense: Impulse-dependent response and the physical properties of asteroids, Acta Astronaut. 166 (2020) 290–305, http://dx.doi.org/10.1016/j.actaastro.2019.10.026, URL: http://www.sciencedirect.com/science/article/pii/S0094576519313323.

[13] L.S. Horan, D.E. Holland, M. Bruck Syal, J.E. Bevins, J.V. Wasem, Impact of neutron energy on asteroid deflection performance, Acta Astronaut. 183 (2021) 29–42, http://dx.doi.org/10.1016/j.actaastro.2021.02.028, URL: https://www.sciencedirect.com/science/article/pii/S0094576521001028.

[14] D.T. Britt, D. Yeomans, K. Housen, G. Consolmagno, Asteroid density, porosity, and structure, in: W.F. Bottke Jr., A. Cellino, P. Paolicchi, R.P. Binzel (Eds.), Asteroids III, University of Arizona Press, 2002, pp. 485–500.

[15] D.J. Scheeres, D. Britt, B. Carry, K.A. Holsapple, Asteroid interiors and morphology, in: P. Michel, F.E. DeMeo, W.F. Bottke (Eds.), Asteroids IV, University of Arizona Press, 2015, pp. 745–766, http://dx.doi.org/10.2458/azu_uapress_9780816532131-ch038.

[16] R. Hupp, S. DeWald, B. Wie, B. Barbee, Suborbital asteroid intercept and fragmentation for very short warning time scenarios, in: Proceedings of the 4th IAA Planetary Defense Conference, International Academy of Astronautics, Frascati, Roma, Italy, 2015, http://iaaweb.org/iaa/ScientificActivity/conf/pdc2015/IAA-PDC-15-03-09ab.pdf, IAA-PDC-15-03-09.

[17] J.P. Sanchez, M. Vasile, G. Radice, On the consequences of a fragmentation due to a NEO mitigation strategy, in: Proceedings of the 59th International Astronautical Congress, Glasgow, United Kingdom, 2008, URL: http://eprints.gla.ac.uk/5053/, IAC-08-C1.3.10.

[18] B. Kaplinger, B. Wie, Orbital dispersion simulation of near-earth object deflection/fragmentation by nuclear explosions, in: Proceedings of the 60th International Astronautical Congress, Daejeon, Republic of Korea, 2009, URL: http://wordpress.engineering.iastate.edu/adrc/files/2012/09/IAC-09.C1.10.2.pdf, IAC-09-C1.10.2.

[19] B. Kaplinger, B. Wie, D. Dearborn, Preliminary results for high-fidelity modeling and simulation of orbital dispersion of asteroids disrupted by nuclear explosives, in: Proceedings of the 2010 AIAA/AAS Astrodynamics Specialist Conference, American Institute of Aeronautics and Astronautics/American Astronomical Society, Toronto, Canada, 2010, http://dx.doi.org/10.2514/6.2010-7982, AIAA-2010-7982.

[20] D. Lee, J.E. Cochran, T.S. No, Orbital dispersion and Earth-impact probability analysis for fragmented asteroids, Aerosp. Sci. Technol. 22 (1) (2012) 24–30, http://dx.doi.org/10.1016/j.ast.2011.05.009, URL: http://www.sciencedirect.com/science/article/pii/S1270963811000824.

[21] J.M. Owen, J.V. Villumsen, P.R. Shapiro, H. Martel, Adaptive smoothed particle hydrodynamics: Methodology. II, Astrophys. J. Suppl. Ser. 116 (2) (1998) 155–209, http://dx.doi.org/10.1086/313100.

[22] J.M. Owen, A compatibly differenced total energy conserving form of SPH, Internat. J. Numer. Methods Fluids 75 (11) (2014) 749–774, http://dx.doi.org/10.1002/fld.3912, URL: https://onlinelibrary.wiley.com/doi/abs/10.1002/fld.3912, arXiv:https://onlinelibrary.wiley.com/doi/pdf/10.1002/fld.3912.

[23] J.J. Monaghan, Smoothed particle hydrodynamics, Rep. Progr. Phys. 68 (2005) 1703–1759, http://dx.doi.org/10.1088/0034-4885/68/8/R01.

[24] J.M. Owen, ASPH modeling of material damage and failure, in: Proceedings of the 5th International SPHERIC SPH Workshop, Manchester, United Kingdom, 2010, URL: https://www.osti.gov/biblio/1009644.

[25] M.B. Syal, J.M. Owen, P.L. Miller, Deflection by kinetic impact: Sensitivity to asteroid properties, Icarus 269 (2016) 50–61, http://dx.doi.org/10.1016/j.icarus.2016.01.010, URL: http://www.sciencedirect.com/science/article/pii/S0019103516000142.

[26] A. Stickle, E. Rainey, M.B. Syal, J. Owen, P. Miller, O. Barnouin, C. Ernst, Modeling impact outcomes for the Double Asteroid Redirection Test (DART) mission, Procedia Eng. 204 (2017) 116–123, http://dx.doi.org/10.1016/j.proeng.2017.09.763, URL: http://www.sciencedirect.com/science/article/pii/S1877705817343217, 14th Hypervelocity Impact Symposium 2017, HVIS2017, 24-28 April 2017, Canterbury, Kent, UK.

[27] M.B. Syal, J. Rovny, J.M. Owen, P.L. Miller, Excavating Stickney crater at Phobos, Geophys. Res. Lett. 43 (20) (2016) 10–595.

[28] W. Schill, J.V. Wasem, J.M. Owen, Modelling and simulation of cratering and ejecta production during high velocity impacts, J. Dyn. Behav. Mater. 3 (2) (2017) 180–188, http://dx.doi.org/10.1007/s40870-017-0094-6.

[29] N. Movshovitz, F. Nimmo, D. Korycansky, E. Asphaug, J. Owen, Disruption and reaccretion of midsized moons during an outer solar system late heavy bombardment, Geophys. Res. Lett. 42 (2) (2015) 256–263.

[30] N. Movshovitz, F. Nimmo, D. Korycansky, E. Asphaug, J. Owen, Impact disruption of gravity-dominated bodies: New simulation data and scaling, Icarus 275 (2016) 85–96, http://dx.doi.org/10.1016/j.icarus.2016.04.018, URL: http://www.sciencedirect.com/science/article/pii/S0019103516300641.

[31] H.J. Melosh, Impact Cratering: A Geologic Process, Oxford University Press, 1989.

[32] G.S. Collins, H.J. Melosh, B.A. Ivanov, Modeling damage and deformation in impact simulations, Meteorit. Planet. Sci. 39 (2) (2004) 217–231.

[33] K. Wünnemann, G. Collins, H. Melosh, A strain-based porosity model for use in hydrocode simulations of impacts and implications for transient crater growth in porous targets, Icarus 180 (2) (2006) 514–527.

[34] M.C. Nolan, C. Magri, E.S. Howell, L.A. Benner, J.D. Giorgini, C.W. Hergenrother, R.S. Hudson, D.S. Lauretta, J.-L. Margot, S.J. Ostro, D.J. Scheeres, Shape model and surface properties of the OSIRIS-REx target asteroid (101955) Bennu from radar and lightcurve observations, Icarus 226 (1) (2013) 629–640, http://dx.doi.org/10.1016/j.icarus.2013.05.028, URL: http://www.sciencedirect.com/science/article/pii/S0019103513002285.

[35] J.H. Tillotson, Metallic Equations of State for Hypervelocity Impact, Technical Report, General Dynamics, General Atomics Division, San Diego, CA, 1962.

[36] N. Lundborg, Strength of rock-like materials, Int. J. Rock Mech. Min. Sci. Geomech. Abstr. 5 (5) (1968) 427–454, http://dx.doi.org/10.1016/0148-9062(68)90046-6, URL: http://www.sciencedirect.com/science/article/pii/0148906268900466.

[37] M. Jutzi, SPH calculations of asteroid disruptions: The role of pressure dependent failure models, Planet. Space Sci. 107 (2015) 3–9.

[38] K.J. Walsh, Rubble pile asteroids, Annu. Rev. Astron. Astrophys. 56 (1) (2018) 593–624, http://dx.doi.org/10.1146/annurev-astro-081817-052013, arXiv:https://doi.org/10.1146/annurev-astro-081817-052013.

[39] R. Managan, K.M. Howley, J.V. Wasem, Efficient and accurate mapping of nuclear-energy deposition, in: Proceedings of the 4th IAA Planetary Defense Conference, International Academy of Astronautics, Frascati, Roma, Italy, 2015, AA-PDC-15-P-53.

[40] W. Benz, E. Asphaug, Catastrophic disruptions revisited, Icarus 142 (1) (1999) 5–20, http://dx.doi.org/10.1006/icar.1999.6204, URL: http://www.sciencedirect.com/science/article/pii/S0019103599962048.

[41] R.L. Ballouz, D.C. Richardson, P. Michel, S.R. Schwartz, Y. Yu, Numerical simulations of collisional disruption of rotating gravitational aggregates: Dependence on material properties, Planet. Space Sci. 107 (2015) 29–35, http://dx.doi.org/10.1016/j.pss.2014.06.003, arXiv:1409.6650.

[42] D. Scott, Multivariate Density Estimation: Theory, Practice, and Visualization, in: A Wiley-Interscience Publication, Wiley, 1992, URL: https://books.google.com/books?id=7crCUS_F2ocC.

[43] E. Feigelson, G. Babu, Modern Statistical Methods for Astronomy: With R Applications, Cambridge University Press, 2012, URL: https://books.google.com/books?id=M6O1yxpvf2gC.

[44] M.A. Wieczorek, M. Meschede, SHTools: Tools for working with spherical harmonics, Geochem. Geophys. Geosyst. 19 (8) (2018) 2574–2592, http://dx.doi.org/10.1029/2018GC007529, arXiv:https://agupubs.onlinelibrary.wiley.com/doi/pdf/10.1029/2018GC007529.

[45] K. Howley, R. Managan, J. Wasem, Blow-off momentum from melt and vapor in nuclear deflection scenarios, Acta Astronaut. 103 (2014) 376–381, http://dx.doi.org/10.1016/j.actaastro.2014.06.022, URL: http://www.sciencedirect.com/science/article/pii/S0094576514002215.

[46] J. Barnes, P. Hut, A hierarchical O(N log N) force-calculation algorithm, Nature 324 (1986) 446–449, http://dx.doi.org/10.1038/324446a0.

[47] L. Hernquist, Performance characteristics of tree codes, Astrophys. J. Suppl. Ser. 64 (1987) 715–734, http://dx.doi.org/10.1086/191215.

[48] M.D. Dikaiakos, J. Stadel, A performance study of cosmological simulations on message-passing and shared-memory multiprocessors, in: Proceedings of the 10th International Conference on Supercomputing, ICS '96, Association for Computing Machinery, New York, NY, USA, 1996, pp. 94–101, http://dx.doi.org/10.1145/237578.237590.

[49] S.J. Aarseth, Dynamical evolution of clusters of galaxies, I, Mon. Not. R. Astron. Soc. 126 (1963) 223, http://dx.doi.org/10.1093/mnras/126.3.223.

[50] E. Hairer, C. Lubich, G. Wanner, Geometric numerical integration illustrated by the Störmer-Verlet method, Acta Numer. 12 (2003) 399–450, http://dx.doi.org/10.1017/S0962492902000144.

[51] V. Springel, The cosmological simulation code GADGET-2, Mon. Not. R. Astron. Soc. 364 (2005) 1105–1134, http://dx.doi.org/10.1111/j.1365-2966.2005.09655.x, arXiv:astro-ph/0505010.

[52] C.D. Murray, S.F. Dermott, Solar System Dynamics, Cambridge University Press, 1999.

[53] E. Jones, T. Oliphant, P. Peterson, et al., Scipy: Open source scientific tools for python, 2001, http://www.scipy.org/, [Online; accessed 2018-10-24].

[54] V.S. Safronov, Evolution of the Protoplanetary Cloud and Formation of the Earth and Planets, Keter Publishing House, 1972.

[55] J. Binney, S. Tremaine, Galactic Dynamics: Second Edition, Princeton University Press, 2008.

[56] E.B. Saff, A.B.J. Kuijlaars, Distributing many points on a sphere, Math. Intelligencer 19 (1) (1997) 5–11, http://dx.doi.org/10.1007/BF03024331.

[57] C. Raskin, J.M. Owen, Rapid optimal SPH particle distributions in spherical geometries for creating astrophysical initial conditions, Astrophys. J. 820 (2016) 102, http://dx.doi.org/10.3847/0004-637X/820/2/102, arXiv:1601.03761.

[58] P. Hut, J. Makino, S. McMillan, Building a better leapfrog, Astrophys. J. Lett. 443 (1995) L93–L96, http://dx.doi.org/10.1086/187844.

[59] D.M. Hernandez, Should N-body integrators be symplectic everywhere in phase space?, Mon. Not. R. Astron. Soc. (2019) http://dx.doi.org/10.1093/mnras/stz884.

[60] B.A. Conway, Optimal interception and deflection of Earth-approaching asteroids using low-thrust electric propulsion, in: M.J.S. Belton, T.H. Morgan, N.H. Samarasinha, D.K. Yeomans (Eds.), Mitigation of Hazardous Comets and Asteroids, Cambridge University Press, 2004, pp. 292–312, http://dx.doi.org/10.1017/CBO9780511525049.015.

[61] B.W. Barbee, Mission Planning for the Mitigation of Hazardous Near Earth Objects (Master's thesis), University of Texas at Austin, 2005.

[62] O.B. Toon, K. Zahnle, D. Morrison, R.P. Turco, C. Covey, Environmental perturbations caused by the impacts of asteroids and comets, Rev. Geophys. 35 (1997) 41–78, http://dx.doi.org/10.1029/96RG03038.

[63] G.S. Collins, H.J. Melosh, R.A. Marcus, Earth impact effects program: A web-based computer program for calculating the regional environmental consequences of a meteoroid impact on earth, Meteorit. Planet. Sci. 40 (2005) 817, http://dx.doi.org/10.1111/j.1945-5100.2005.tb00157.x.

[64] J.D. Hunter, Matplotlib: A 2D graphics environment, Comput. Sci. Eng. 9 (3) (2007) 90–95.

[65] H. Childs, E. Brugger, B. Whitlock, J. Meredith, S. Ahern, D. Pugmire, K. Biagas, M. Miller, C. Harrison, G.H. Weber, H. Krishnan, T. Fogal, A. Sanderson, C. Garth, E.W. Bethel, D. Camp, O. Rübel, M. Durant, J.M. Favre, P. Navrátil, VisIt: An end-user tool for visualizing and analyzing very large data, in: High Performance Visualization–Enabling Extreme-Scale Scientific Insight, 2012, pp. 357–372.

[66] Wolfram Research, Inc., Mathematica, version 10.3, 2015, Champaign, IL..